nature chemical biology

Article

https://doi.org/10.1038/s41589-025-02032-w

Molecular basis for the regulation of membrane proteins through preferential lipid solvation

Received: 8 March 2025

Accepted: 27 August 2025

Published online: 26 September 2025

Check for updates

Nathan Bernhardt[1], Tugba N. Ozturk[1,2], Shan Zhang[1], Noah Schwartz[1], Rahul Chadda[2], Alejandro Gil-Ley[1], Janice L. Robertson[2] ✉ & José D. Faraldo-Gómez[1] ✉

The mechanism by which lipids regulate membrane proteins remains an open question. While many protein structures reveal associated lipids, neither binding nor regulatory mechanisms can be gleaned from frozen static snapshots, as these processes occur in the context of a dynamic membrane at equilibrium. In this study, we combine single-molecule experiments with computational analyses of lipid dynamics and lipid-solvation energetics to understand how changes in the lipid composition of the membrane influence the dimerization of the CLC-ec1 chloride/proton antiporter. We find this influence does not result from long-lived lipid binding at specific sites, but instead from an inherently dynamic effect known as preferential lipid solvation, which ultimately determines the relative thermodynamic stability of associated and dissociated dimers. This study provides a foundation for linking lipid composition to the modulation of membrane protein conformational equilibria and a framework for discriminating among different lipid regulation mechanisms in membranes.

The chemical composition of biological membranes is extraordinarily diverse, varying radically across different organisms, cell types and organelles. This complexity allows membranes to form stable, fluid lipid bilayers across a wide range of environmental conditions. Yet, this variability appears excessive beyond necessity, indicating that lipids may participate in other important physiological roles, such as protein regulation[1,2]. Indeed, numerous experimental studies of membrane protein activity over the past two decades have demonstrated marked dependencies on the specific lipid composition of the membrane[3–6].

Variations in lipid composition can change the membrane in different ways. Large variations may alter its macroscopic structural and mechanical properties, such as thickness, intrinsic curvature or elasticity. Continuum mechanics models have been highly successful at capturing these phenomena and illustrating how the conformational energetics of proteins and membranes are inextricably linked[7]. When bulk changes in the membrane are minor or not apparent, however, the nature of the coupling between protein equilibria and lipid composition has been more difficult to rationalize. Indeed, changes in lipid content in cells are typically adaptive and occur at relatively modest levels, preserving the overall structure and fluidity of their membranes[8,9]. In many cases, therefore, lipid-dependent effects on protein activity are local and specific, and thus beyond the continuum mechanics approximation. To conceptualize these effects, it is instead helpful to recognize the following two facts: first, that the lipid membrane is a fluid layer of discrete molecules in constant flux, solvating the membrane proteins embedded within; and second, that membrane protein surfaces are often highly irregular, both geometrically and chemically, and optimal solvation thereof might entail substantial adaptations in

[1]Theoretical Molecular Biophysics Laboratory, National Heart, Lung and Blood Institute, National Institutes of Health, Bethesda, MD, USA. [2]Department of Biochemistry and Molecular Biophysics, Washington University School of Medicine, St. Louis, MO, USA. ✉e-mail: janice.robertson@wustl.edu; jfg4wrk@gmail.com

the spatial distribution of the lipid types present in the membrane[10]. In this microscopic view, the conformational equilibrium of a protein is influenced by the lipid composition of the membrane because the latter dictates the energetics of lipid solvation for each of the protein states[11]. It is worth noting that this microscopic perspective can be connected to the continuum mechanics description, either through the use of atomistic knowledge to construct improved models[12,13], or ideally through the derivation of free-energy functionals from analysis of molecular ensembles of lipids in different states, thereby providing an all-scale understanding of membrane structure and energetics[14,15].

A growing collection of data derived from mass spectrometry[16,17] and cryo-electron microscopy[18–22] has inspired an alternative perspective of molecular-scale lipid effects. In this view, individual lipids become immobilized in complexes with a target protein, favoring certain functional states, due to long-lived intermolecular interactions at specific sites on the protein surface, with lipid headgroups likely conferring specificity. While this notion is plausible in some circumstances, it is worth noting that these experimental approaches examine protein–lipid interactions out of context, that is, not a dynamic lipid bilayer at equilibrium. This concern is often set aside under the assumption that these types of experiments capture the most probable snapshot of the system in the original equilibrium state. The fact is, however, that the act of isolating a protein is not instantaneous but happens over a timescale that is slow compared to lipid diffusivity and rotational motion, and so these experiments are more likely to capture the most probable snapshot of the perturbed condition, which may or may not coincide with that in an actual thermalized membrane. Based on this, it is not evident which interactions are truly mechanistically significant, and which are spuriously induced, or at least enhanced. The appearance of binding can arise from other mechanisms, such as artifactual association[23] or weak solvation effects[24,25]. The mechanism at play in each case must be examined through the prism of linkage thermodynamics, which describes how binding of one molecule or species exerts an effect on another reaction[26], and requires equilibrium titration studies[27]; it follows that membrane protein reactions must therefore be studied inside lipid bilayers. For example, site-specific binding features the characteristic saturation of the bound state as a function of ligand concentration, whereas weak linkage effects such as preferential solvation do not. As lipids have the potential to act as both solvents and ligands, it is essential to distinguish between these distinct mechanisms to understand how lipids modulate membrane proteins within membranes.

Unfortunately, there exists limited thermodynamic data reporting on changes in membrane protein equilibria in membranes linked to the molecular activity of lipids. Our recent studies on the dimerization energetics of CLC-ec1 (refs. 28,29), a prokaryotic chloride–proton antiporter in lipid bilayers, provide access to this critical information. This reaction is a prototype of a pervasive process in membrane physiology: protein oligomerization. It is also one of the few examples for which thermodynamic linkage between protein structure and lipid activity has been experimentally established[25,30,31]. Like other self-organization processes in the membrane such as the dimerization of inverted-topology subunits to form the fluoride selective Fluc channel[32], the assembly of ATP synthase dimers into rows to form mitochondrial cristae[33], and the clustering of the core autophagy membrane protein ATG9A[34], dimerization of CLC-ec1 is in part due to a morphological perturbation in the lipid bilayer created by the monomeric protein, which is relieved upon association[25] (Fig. 1). The cause of this perturbation is a specific feature on the protein surface formed by atypically short transmembrane α-helices flanked by ionized and polar residues, which create a local region of hydrophobic mismatch. Adequate solvation of this region requires lipids in its vicinity to become strongly tilted and entangled, resulting in a thinning of the membrane by as much as one-third of the bulk length. Because this defect disappears in the dimer, it translates into a driving force for protein–protein association that arises from the membrane. That is, dimerization is favored from a net gain in the conformational free-energy of the membrane, in addition to the gain resulting from contacts at a complementary protein–protein interface. Considering the membrane as a solvation structure builds upon the foundation of continuum membrane modeling, providing a necessary molecular-scale connection that bridges these methods to consider chemical complexity.

Consideration of membrane coupling through changes in solvation free energies also provides an intuitive way to understand the coupling of membrane protein reactions to lipid composition, aligning more closely with our understanding of the stability of soluble proteins. Indeed, this is also observed in the dimerization equilibrium of CLC-ec1, as the monomer-dimer population observed in 1-palmityl-2-oleoyl-sn-glycero-3-phosphoethanolamine (POPE) and 1-palmityl-2-oleoyl-sn-glycero-3-phosphoglycerol (POPG) membranes are shifted upon addition of shorter C12:0 acyl chain lipids, 1,2-dilauroyl-sn-glycero-3-phosphoethanolamine (DLPE) and 1,2-dilauroyl-sn-glycero-3-phospho-(1'-rac-glycerol) (DLPG). Our measurements revealed that DLPE/DLPG lipids substantially inhibit dimerization without compromising structure or antiport activity. Remarkably, this effect was detectable even for DL/PO ratios much smaller than 1% and showed no saturation with increasing DL. Coarse-grained (CG) molecular dynamics (MD; combined known as CGMD) simulations of CLC-ec1 monomers in mixtures of POPE/POPG and DLPE/DLPG lipids revealed sequestering of DLPE/DLPG lipids near the exposed dimerization interface for all concentrations considered, in line with the nonsaturating impact on the free energy changes experimentally observed. The evidence so far is compelling but only infers the mechanism of preferential solvation. We still lack the connection of how molecular changes in the membrane lead to thermodynamic changes in oligomerization. Specifically, how does burial of the membrane defect incur the energetic impact to drive dimerization? Furthermore, how do we distinguish DL enrichment as a weak solvation effect rather than site-specific binding, and how does enrichment translate to energetic changes in the self-assembly of subunits?

Here we address these questions by conducting an integrated study that combines experiments and theoretical calculations. We first measure the dimerization of CLC-ec1 in bilayers with net neutral phosphocholine (PC) headgroups, revealing that DL inhibition persists with different headgroups and does not depend on specific protein–headgroup interactions. We then use three different applications of the MD simulation method to dissect the molecular mechanism of DL inhibition of dimerization. First, we calculated an all-atom 40-microsecond MD trajectory of a CLC-ec1 monomer in 1-palmitoyl-2-oleoyl-glycero-3-phosphocholine (POPC)/1,2-dilauroyl-sn-glycero-3-phosphocholine (DLPC) and deployed an advanced lipid dynamics analysis method to reveal how short-chain lipids become enriched at the dimerization interface without long-lived binding. Second, we developed a protocol to calculate, with high statistical precision, the change in total solvation free energy of a membrane protein upon global changes in lipid composition. We used this protocol to compare the solvation free energies of monomeric and dimeric CLC-ec1 in POPC versus POPC/DLPC using a CG representation, recapitulating our experimentally measured changes in dimerization free energy. Finally, we developed a methodology to evaluate the energetics of CLC-ec1 dimerization before the formation of direct protein–protein interactions and investigate how DL lipids influence the driving force generated by the membrane. Ultimately, we uncover experimental and computational evidence that changes in membrane solvation energetics drive CLC dimerization, with lipids modulating the magnitude of the energy differences without long-lasting protein–lipid interactions. We posit that preferential solvation thermodynamics enables cells to harness the astounding chemical complexity of lipid membranes to regulate the conformational equilibria of proteins therein, thereby tuning their functional activity across various conditions.

https://doi.org/10.1038/s41589-025-02032-w

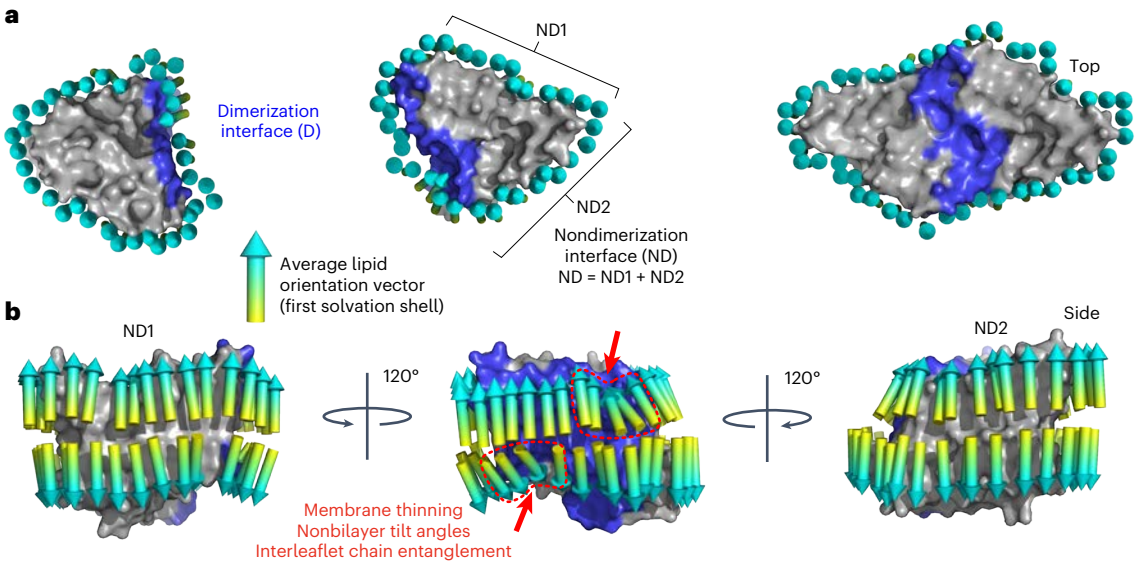

Fig. 1 | Solvation shell lipids exhibit orientation defects along the dimerization interface of CLC-ec1. a, The CLC-ec1 Cl^-/H^+ antiporter forms a dimer complex, whereupon dimerization removes about 20 lipids from the annular solvation shell that return to the bulk. The average lipid orientation in the first solvation shell is depicted as an orientation vector relative to the bilayer normal, plotted using previous CG simulation data[25]. Please note that arrows reflect directional vectors of lipid orientation along the membrane lattice points and not whole lipids. **b**, In the monomeric state, CLC-ec1 perturbs the surrounding membrane structure around the dimerization interface, D, resulting in increased lipid tilt angles, chain entanglement, and a reduction of the membrane thickness adjacent to this surface. Burial of this interface eliminates the defect completely, exposing the remaining nondimerization surfaces, ND = ND1 + ND2, where the lipids adopt bulk-like bilayer orientations.

Results

CLC-ec1 dimerization is inhibited by short-chain PC lipids

In previous experiments, we found that addition of DLPE/DLPG lipids to POPE/POPG membranes inhibits CLC-ec1 dimerization[25]. Analysis of lipid distributions around the protein by CGMD simulations indicates that this effect stems from the enrichment of short-chain DL lipids at the binding interface that becomes exposed upon dissociation. However, the mechanism governing this enrichment remains unclear and could result from site-specific binding at the interface. One of the elements of this lipid-as-ligand association mechanism is that chemical specificity is imparted by persistent interactions between the lipid headgroup and the protein, which may be potentiated when lipids carry a net charge. Indeed, our original studies included changing the amount of negatively charged POPG and DLPG lipids. To examine this further, we investigated whether DL enrichment around CLC-ec1 is specific to this headgroup by repeating the analysis in pure POPC and a mixture of 80% POPC/20% DLPC. Under these conditions, we observe a similar membrane thinning in the net neutral lipid bilayers (Fig. 2a and Extended Data Fig. 1a), as well as the same degree of DL enrichment (Fig. 2b and Extended Data Fig. 1b). This indicates that the effects observed in our MD simulations are driven by the shorter acyl chains, and not by the lipid headgroups.

Next, we experimentally investigated whether DLPC inhibits CLC-ec1 dimerization on the background of POPC membranes. To achieve this, we used a method known as single-molecule subunit capture, which measures equilibrium oligomerization in membranes by analyzing the density-dependent Poisson-like statistical distribution of fluorescently labeled protein subunits captured into liposome membrane fractions[30,35,36]. Randomly dispersed monomers in the membrane would tend to be captured into many liposomes during extrusion, while the same amount of protein assembled into higher-order oligomers is expected to occupy fewer liposomes and with higher subunit numbers per vesicle. The fluorophore-labeled subunit occupancy is measured directly by single-molecule photobleaching analysis, and the photobleaching probability distributions of fluorescently labeled protein captured into liposomes, (P_1, P_2, P_{3+}), reports on the oligomeric population in the pre-extruded membrane. This method has been extensively validated and previously used to report on the dimerization equilibrium of CLC-ec1 (refs. 30,35,36), and the Fluc-Bpe F^- channel[32]. In the current study, we used this approach to measure CLC-ec1 dimerization in the different headgroup composition of PC. In 100% POPC, the photobleaching probability distributions are like those in 2:1 POPE/POPG, confirming that the protein is mainly dimeric at the mole fraction density of 1 subunit per 10^6 lipids in both PO compositions (Fig. 2c). However, addition of 20% DLPC increases the proportion of single photobleaching steps, indicating a substantial shift towards monomers, like what was observed previously for DLPE/DLPG lipids. To rule out whether the increase in apparent monomers arises from off-pathway states, such as subunit misfolding, we interrogated the proteoliposomes for their chloride transport function. Indeed, transport is observed in both membrane compositions and is enhanced in the presence of DLPC, indicating that the subunits remain actively folded (Fig. 2d,e). From this, we conclude that the increased probability of single photobleaching steps in the DL-supplemented PC membranes indicates an increase in functional CLC-ec1 monomers in the protein population. These results provide experimental evidence that the inhibitory effect of DL lipids on CLC-ec1 dimerization is due to chain length, rather than protein–headgroup interactions.

Lipid exchange biases lead to DL enrichment at the dimer interface

If DL enrichment does not involve specific headgroup interactions, then why do DL lipids accumulate at the dimerization interface? Counterintuitively, it is possible that shorter acyl chains form more interactions with the protein if they fit into specific pockets that are not accessible by longer PO. As experimental methods about lipid dynamics near proteins are limited, we turn to all-atom MD simulations to provide insights not otherwise attainable. While CG force fields permit high-quality statistics useful for examining membrane morphology[32,37], all-atom force fields are the method of choice to evaluate close-range protein–lipid interactions and dynamics. It is crucial, however, that the calculated trajectories are much longer than the characteristic diffusion times of lipids, both in the

https://doi.org/10.1038/s41589-025-02032-w

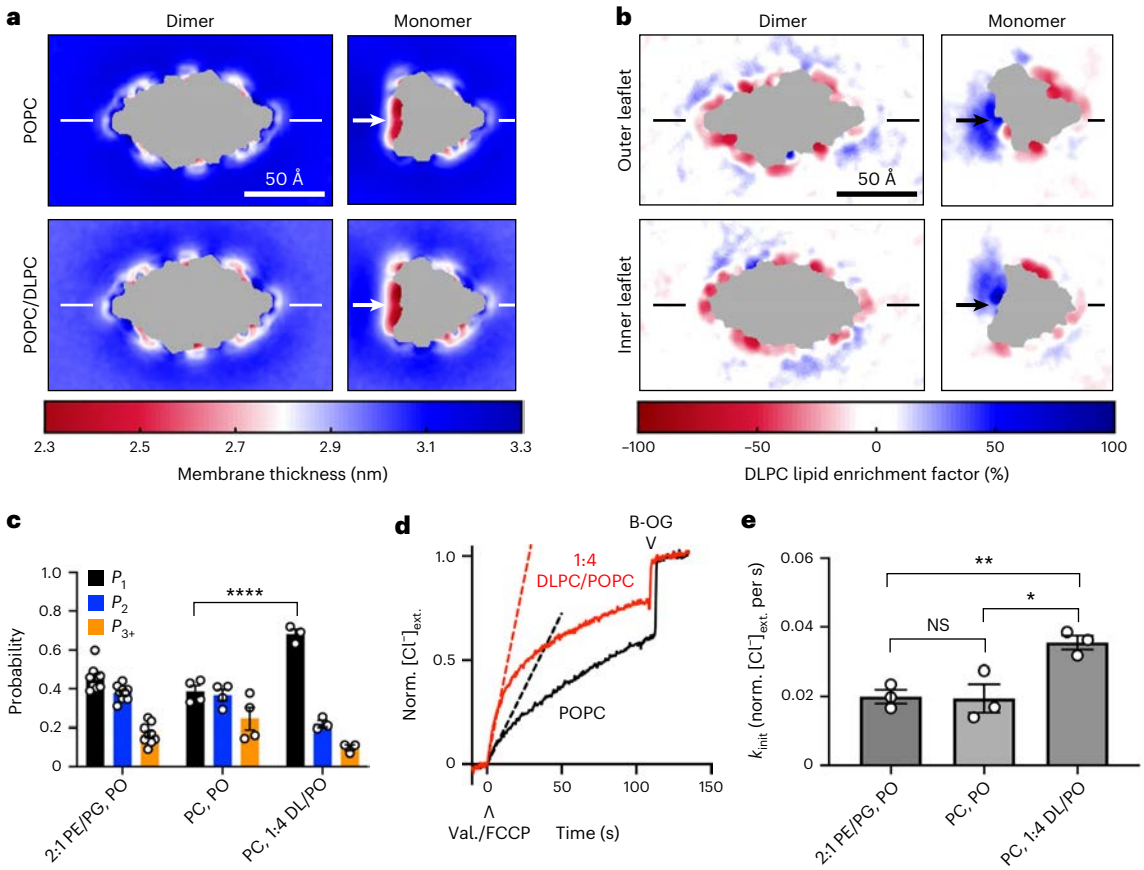

Fig. 2 | DLPC inhibition of CLC-ec1 dimerization. a, Membrane thickness maps of the CLC-ec1 dimer and monomer subunit in POPC and 20% DLPC/80% POPC lipid bilayers, both calculated from 40 µs CGMD simulations with the MARTINI force field, respectively. **b**, DLPC enrichment at the dimerization interface. **c**, Single-molecule photobleaching probability distributions (P_1, P_2, P_{3+}) of CLC-ec1-Cy5 at 0.1 µg mg^{-1}, $\chi_{reconst.} = 10^{-6}$ subunits per lipid in 2:1 POPE/POPG, POPC and 1:4 DLPC/POPC membranes. P_1 represents the probability of observing single photobleaching steps, P_2 represents double steps and P_{3+} are spots that bleached in three or more steps. Data represent mean ± s.e.m. for $n = 9$, 4 and 3 biological replicates for 2:1 POPE/POPG[25], POPC and 1:4 DLPC/POPC samples, respectively, imaged 2–5 days after freeze/thaw fusion. A two-tailed χ^2 test was carried out on the different distributions: POPC versus 2:1 POPE/POPG, not significant (NS), $P = 0.0872$; POPC versus 1:4 DLPC/POPC, ****$P < 0.0001$. **d**, Raw chloride efflux trace from a 1 µg mg^{-1}, $\chi_{reconst.} = 10^{-5}$ subunits per lipid reconstituted in POPC (black) or 1:4 DLPC/POPC (red). The upward caret (^) indicates initiation of transport with valinomycin and FCCP, whereas the downward caret (v) indicates addition of detergent β-OG, releasing the remaining trapped chloride within the proteoliposomes. Dashed lines indicate linear fits of the first 10 s of transport, to determine k_{init}. **e**, Rate of chloride transport from proteoliposomes, k_{init} (norm. $[Cl^-]_{ext.}$ per s). Data represent mean ± s.e.m. for $n = 3$ biological replicates for each lipid composition. Unpaired two-tailed t tests carried out between DL and PO conditions: POPC versus 1:2 POPE/POPG, NS, $P = 0.9132$; POPC versus 1:4 DLPC/POPC, *$P = 0.0243$; 2:1 POPE/POPG versus 1:4 DLPC/POPC, **$P = 0.0052$.

bulk and near proteins. To examine whether the inhibitory effect of DL lipids on CLC-ec1 oligomerization reflects long-lived DL binding events at the dimer interface, we calculated a 40-µs MD trajectory for a CLC-ec1 monomer immersed in a 70% POPC/30% DLPC mixture on an Anton 2 supercomputer using a well-calibrated force field. Lipid dynamics were analyzed using MOSAICS[38], a comprehensive software suite specifically designed for time- and space-resolved analyses of membrane structure and dynamics in multicomponent systems. Among many other descriptors, MOSAICS facilitates a quantitative evaluation of lipid mixing in multicomponent bilayers; this insight is necessary because it reveals whether the length of a given trajectory is sufficient to eliminate spurious effects due to the starting condition of the simulation. Nearly complete mixing of POPC and DLPC occurs over the 40-µs trajectory with converged mean lipid-solvation numbers for both species (Fig. 3a). This high degree of sampling allowed for the quantification of lateral diffusion constants for each species (Fig. 3b), demonstrating the characteristic timescale required for the emergence of molecular Brownian motion (about 50 ns), as opposed to in-place fluctuations. Analyzing the macroscopic membrane structure that emerges from this dynamic system, we see that the membrane thickness (Fig. 3c) and DL enrichment at the dimerization interface (Fig. 3d) recapitulate what we observed in our CGMD simulations of membranes with PG/PE headgroups[25].

Through Voronoi tessellations of every snapshot, we tracked each lipid type (Fig. 4a) and the area it occupies to analyze timescales of lipid occupancy mapped onto the 2D lattice (Fig. 4b). These trajectories illuminate the mechanism of Brownian motion of lipids (Supplementary Video 1)—lipids act as amorphous blobs, exchanging with their neighbors without generating empty spaces in the process. In the bulk, lateral displacements are isotropic and rapid, but on the protein, lipids slide along the surface only returning to the bulk after being displaced by a neighboring lipid. These observations suggest that protein shape is the most crucial factor determining the dwell time of a given lipid molecule, since a pocket would protect it from being replaced by its neighbors. However, such pockets are absent on the surface of CLC-ec1 and turnover of lipids at the protein is constant. By 40 µs, 99% of all lipids have exchanged into the first solvation shell with both PO and DL lipids participating in this nonstop turnover along the entire perimeter of the protein (Extended Data Fig. 2a).

Analysis of lipid dynamics at the protein surface indicates that DL enrichment at the dimer interface is not due to long-lived association.

https://doi.org/10.1038/s41589-025-02032-w

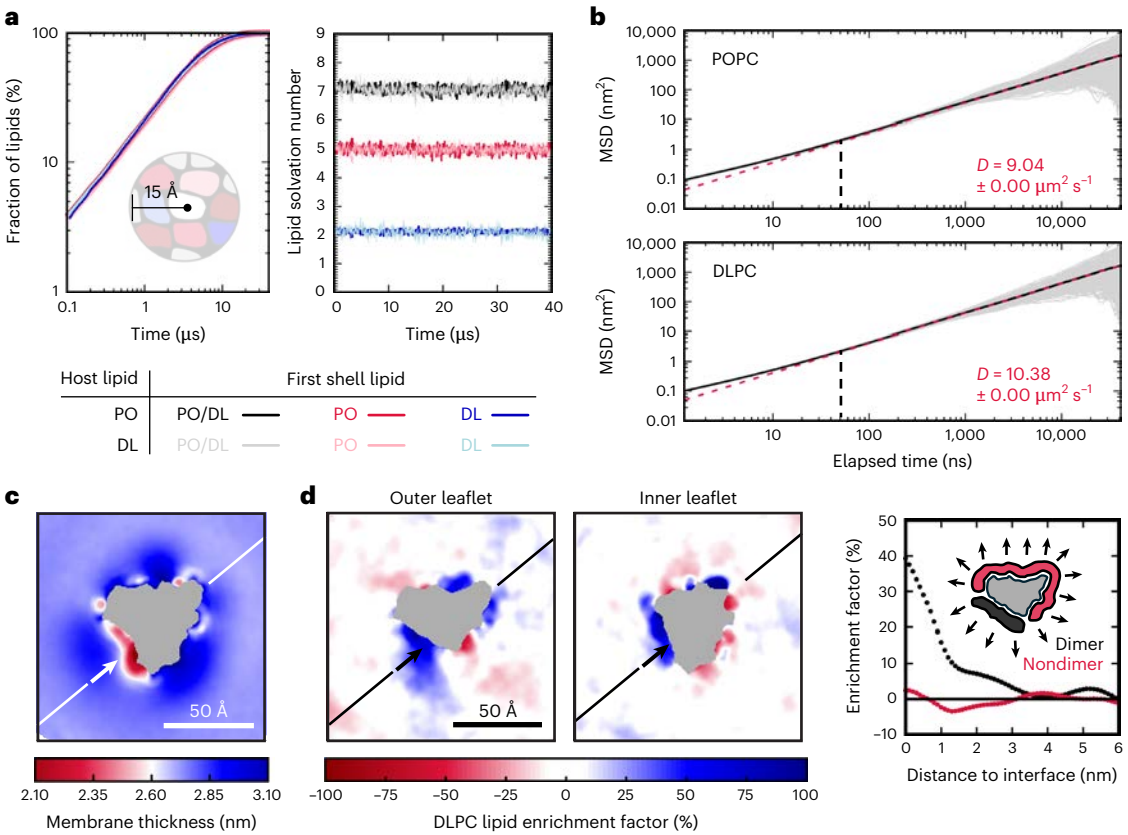

Fig. 3 | Lipid sampling around the CLC-ec1 monomer in DLPC/POPC membranes. From 40-μs all-atom MD simulations run on Anton 2 using the CHARMM36m force field. **a**, Left: fraction of lipids visiting the first solvation shell defined within a 15 Å cutoff distance for all PO and DL lipids (inset). Right: lipid solvation number for the first solvation shell of either PO or DL. Each lipid is analyzed over a 50 ns window and spurious solvation events (<25 ns) are ignored, depicted as uncolored lipids on the outside periphery of the inset. Data averaged over all lipids in the molecular system. **b**, MSD versus simulation time. Gray lines show individual lipid data, while black lines show the average over all lipids. Least squares regression (red dashed line) excludes nonlinear data, that is, <50 ns, yielding estimation of the diffusion coefficient, $D \pm$ error of fit. **c**, Membrane thickness map measuring distances between carbonyl carbons on each leaflet. Gray regions represent low lipid density that roughly corresponds to the protein's location. The dimerization interface is indicated with an arrow and its perpendicular axis is designated with a line. **d**, Left: DLPC lipid enrichment factor map for each leaflet. Right: average enrichment factor over both leaflets for the dimerization versus nondimerization interface.

The number of visits (Fig. 4c) and mean residence times (Fig. 4d) indicate that lipids are constantly in a dynamic exchange at the protein surface. Average residence times are 60–80 ns, with some 'hot-spots' exhibiting longer dwell times, but these do not exceed 500 ns on average, our cutoff for considering a lipid to be long-lived. Notably, hot-spots do not discriminate between PO or DL. There is a strong correlation between mean residence time and total number of protein–lipid contacts (Fig. 4e), with the inner leaflet showing longer dwell times, likely due to the increased number of salt bridges (Fig. 4f and Extended Data Fig. 3) while hydrogen bonds are similar in both leaflets (Fig. 4g). Focusing on the first solvation shell, the residence times are distributed according to a power law (Extended Data Fig. 2b,c), following what has been reported for CG models[39], with the mean DL residence times being approximately 9 ns longer than those of PO at the dimerization interface and PO residence times increasing at the membrane-facing surface (Fig. 4h). These differences translate into 7 ± 5 % DL enrichment, far lower than what we observe.

While not inconsequential, dwell-time differentials do not explain our 2D-projection data, and so we surmise that DL enrichment must occur due to an increase in DL entry into the first solvation shell. To examine this hypothesis, we calculated the exchange probabilities of lipids into the first and second solvation shells by pairing each lipid that leaves one shell with one that enters from the outside (Fig. 4b,i, Extended Data Fig. 2i,j and Supplementary Table 1). At all protein surfaces, there is a preference for DL molecules to enter the first and second solvation shells, but this effect is amplified at the thinned dimerization interface, where DL molecules are 5 ± 1% more likely to enter the first shell than expected (Supplementary Table 2). This contributes an enrichment of 26 ± 6% due to increased entry of DL, and together with the enrichment due to DL retention, we calculate an overall 35 ± 12% in DL enrichment, consistent with values obtained from 2D-projection data (Fig. 3d). This analysis is also consistent at the nondimerization interface, which exhibits a small exchange preference for DL that is offset by shorter dwell times compared to PO resulting in neutral lipid selectivity (Supplementary Tables 2–4). Therefore, enrichment of DL lipids at the CLC-ec1 dimerization interface is not explained by specific, long-lived lipid binding, but by the balance of lipid-lipid exchange and dwell times that are dependent on membrane morphology.

Differentials in lipid solvation energies explain DL inhibition

How does DL enrichment energetically decrease CLC-ec1 dimerization stability? To answer this question, we calculated the change in solvation free energy between the CLC-ec1 monomer and dimer states, coupled to lipid composition. We adapted a simulation methodology designed to evaluate differential binding energetics for small molecules, known as the free-energy perturbation (FEP) approach[40]. Typically, a solute is gradually transformed into another as the simulation progresses, while the solvent, for example, water, or a binding pocket, remains unchanged; the resulting energetic change is then extracted from the simulated trajectory. Here, we used this 'alchemical' approach, paired

https://doi.org/10.1038/s41589-025-02032-w

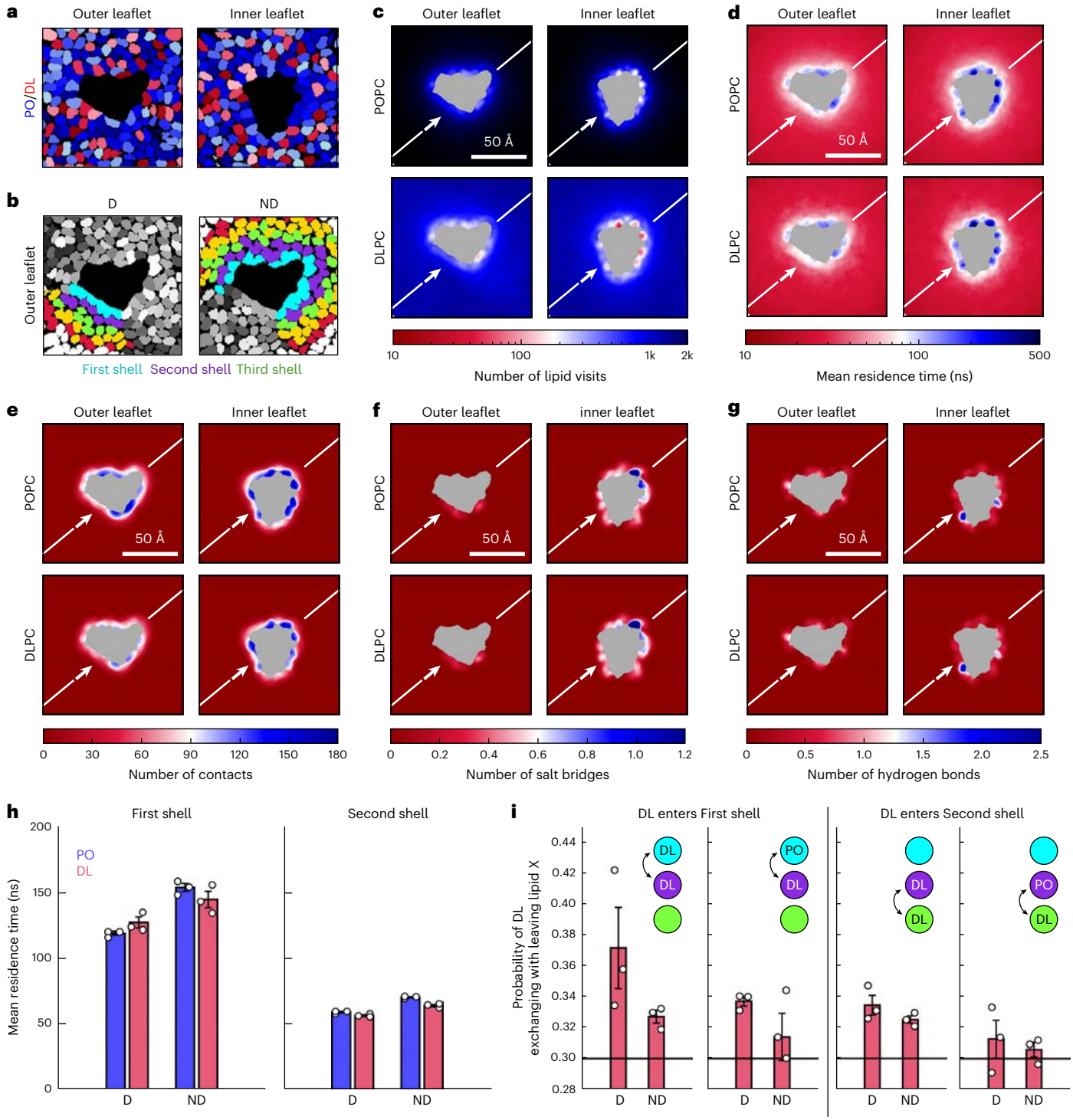

Fig. 4 | Lipid residence and exchange dynamics around the CLC-ec1 monomer in DLPC/POPC membranes. From all-atom MD simulations run for 40 µs on Anton 2 using the CHARMM36m force field. **a**,**b**, Precise characterizations of the dynamics are obtained through spatial mapping onto a 2D grid, depicted by Voronoi tessellation analysis. With this, lipid species (for example, PO (blue) versus DL (red)) can be categorized into larger structures (**a**), like the first and second solvation shells shown in cyan and purple, respectively, in regions sitting adjacent to either the dimer or nondimer interface (**b**). **c**, Number of lipid visits in the mean residence time calculation. **d**, Mean lipid residence time obtained from Voronoi tessellation data. **e**, Total contact number between each lipid type and the CLC-ec1 subunit, where a contact is counted as any atom pair with a separating distance <3.5 Å. **f**,**g**, This is further categorized as salt bridge (**f**) or hydrogen bond contacts (**g**; Extended Data Fig. 3a,b). **h**, Mean residence times of lipids in the first and second solvation shells determined from 2,289 PO and 1,234 DL lipid visits to the dimer interface, and 5,811 PO and 2,699 DL visits to the nondimer interface (Supplementary Table 1). Data represent mean ± s.e.m. for $n = 3$ technical replicates, obtained by splitting the full trajectory into 3×13.3 µs nonoverlapping segments and calculating the mean residence time from each individual segment (overlaid scatter points). **i**, Probability of DL exchanging with a leaving lipid (X = DL or PO) for the first (cyan) and second (purple) solvation shells (as depicted in **b**), averaged over both leaflets. Conversely, the PO exchange probabilities are equal to 1-DL exchange probabilities (Extended Data Fig. 2i,j). Data represent mean ± s.e.m. for $n = 3$ technical replicates calculated from each trajectory segment. D, dimer; ND, nondimer.

with a CG model, to transform not just one solute but hundreds of lipids, thereby altering the total composition of the membrane. We select POPC lipids that are randomly positioned within the bilayer and 'morph' them into DLPC (Fig. 5a), in both the dissociated and associated states of CLC-ec1, as well as the protein-free membrane as a reference. For each POPC to DLPC conversion, there is a reduction in the chain length by one bead, but also a change in chain saturation and final chain energy terms. Starting out with 100% POPC, we evaluated incremental changes in the DLPC molar fraction, ranging from 1 to 30% in discrete steps (Fig. 5b). Morphologically, these transformations yield consistent results where DL lipids become spontaneously enriched at the dimerization interface at all DL/PO ratios while PO lipids are preferred elsewhere around the protein perimeter (Extended Data Fig. 4). A 10% change in the DL/PO ratio corresponds to 110 lipid molecules transformed from POPC to DLPC; as a result, the free-energy cost of the global transformations is large, on the order of 500 kcal mol^{-1} for a 10% change (Fig. 5c). In contrast, the solvation free energy changes, that is, the difference in energy between the protein versus membrane alone, only differ by a fraction of 1 kcal mol^{-1}, with sufficiently small errors indicating convergence of the calculations over these long sampling times (Fig. 5d).

This approach enables us to calculate how the free energy of solvating each state depends on DL. The cost of solvating the dimer increases by 1 kcal mol^{-1} at 30% DL, while the opposite trend is observed for the monomeric state; at all increments, the free-energy cost of solvating dissociated subunits in DL is lower than the protein-free bilayer, with −1.5 kcal mol^{-1} at 30% DL. Therefore, there are two factors contributing to DL inhibition of CLC-ec1 dimerization. First, the mixed DL/PO membrane is an energetically better solvent for the monomer, as DL is better matched to the morphological defect at the dimerization interface. Second, the pure PO membrane is a better solvent for the dimer, as PO lipids are better matched to the rest of the protein-membrane interface. Considering both contributions, we calculate a net destabilization of dimerization by −2.5 kcal mol^{-1} in 30% DL, agreeing with our past experimental results and supporting a mechanism of preferential solvation[25] (Fig. 5e and Extended Data Fig. 5).

Burial of the membrane defect confers orientational specificity

The above analysis shows that changes in lipid-solvation energies explain why DL lipids inhibit CLC dimerization. It is essential to note that these calculations do not account for contributions from protein–protein interactions in the dimer, indicating that changes in membrane energetics drive complex formation before the subunits come into contact. To examine this hypothesis, we designed a series of CG simulations wherein two monomers are gradually brought together but prevented from forming protein–protein interactions by an artificial repulsive force that is activated only when subunits are in close range, that is, providing a 'bumper' around the protein perimeter that limits protein contacts (Fig. 6a). Under these conditions, we calculated the free energy difference of bringing subunits close to one another in the membrane using the umbrella sampling method and examined the dependency of the free energy change on protein orientation and lipid composition. As a negative control, we examined the reaction in a non-native orientation where subunits are rotated so that dimerization interfaces face away from each other and the membrane defects remain exposed in all states (Fig. 6b). The free-energy profile shows that in this orientation it is unfavorable to bring subunits close to one another (Fig. 6c). However, when the subunits approach in the native orientation, we obtain a favorable free energy for formation of a 'precomplex' dimer that does not involve protein–protein interactions.

The features of the dimerization energy profile can be linked to changes in membrane morphology at different intersubunit separations. In the fully dissociated state (that is, center-to-center intersubunit distance around 9 nm) each subunit forms a membrane defect at the dimerization interface, with bulk-like bilayer in between (Fig. 6b). As the subunit distance is decreased to 6 nm separation, the free energy steadily increases unfavorably to 3 kcal mol^{-1}, where the defects occupy a larger area than when the monomers are farther apart. As the subunits are brought closer still, the free energy decreases sharply as the two defects coalesce, and the affected membrane area becomes smaller. At 4.3 nm separation, only a single layer of lipids remains between the two subunits (Extended Data Fig. 6c), with only 2% of protein–protein contacts observed in the dimeric structure of CLC-ec1 formed (Fig. 6d). This 'precomplex' state is −2 kcal mol^{-1} more stable than the dissociated state and indicates that association at the native dimerization interface is favorable even in the absence of protein contacts. These results also show that the membrane defect confers orientational specificity to the reaction, potentially enabling the driving of subunit association at a distance.

Consistent with our previous findings, the free energy of 'precomplex' formation is destabilized in the PO/DL membrane, with a modest free-energy gain of −0.6 kcal mol^{-1} relative to the dissociated form (Fig. 6c). Taking the difference between PO and PO/DL conditions, addition of the short-chain lipids destabilizes dimerization by 1.4 kcal mol^{-1}. Elimination of the remaining lipids would further enhance this inhibitory effect, as POPC chains are unfavorable at the dimerization interface. However, the final de-lipidation step is inherently coupled to the formation of many protein–protein contacts and so it is not possible to evaluate the energetics of these two processes separately. Still, these results demonstrate the dependency of the dimerization free energy on short-chain DL lipids, showing that changes in membrane composition can modulate the energetics of membrane protein association, and this effect does not require protein–protein interactions.

Discussion

This study combines experiments with computational methodologies to uncover the mechanism by which the lipid composition of the membrane influences the oligomerization of the CLC chloride/proton antiporter. This effect originates from the structure of the CLC subunit, which features a region on its transmembrane surface that is lipophilic but atypically thin and curved, resulting in a hydrophobic mismatch with the membrane. Adequate solvation of this surface results in a perturbation to the surrounding lipid bilayer structure, and C16/C18 biological lipids end up tilted with reduced packing (Fig. 1). While this is a stable solvation structure, lipids are energetically frustrated here compared to the bulk, resulting in a relative energetic penalty for solvating the monomer. Dimerization is thus energetically favored because it eliminates this mismatched protein–lipid interface, allowing up to 20 lipids to return to the bulk–bilayer configuration. Accordingly, our potential-of-mean-force calculations show that CLC dimerization is only favored when it involves the protein surface that accompanies the membrane defect (Fig. 6). While protein–protein contacts are expected to contribute to the dimer stability at close range, we find that it is the generalizable changes in membrane energetics that drive the subunits to come close to one another, in a specific orientation, and form specific precomplex states. This effect has also been observed in other systems. The homodimeric F^- ion channel Fluc exhibits a similar membrane defect that is formed by hydrophobic mismatch at charged surfaces[32]. In fact, the magnitude of Fluc dimerization affinity is remarkably like that of CLC-ec1, potentially due to the similarity in membrane defect shape and size. Thinned membrane defects are also observed in membrane proteins that participate in dynamic association with protein cargo, such as insertases[41–43], indicating that the driving force for protein association in those cases might also result from elimination of energetically frustrated lipid-solvation shells, offering a way of imparting affinity to these complexes without the need for strong protein interactions.

The observation that changes in membrane energetics drive CLC dimerization extends from other studies that have shown that membrane proteins associate to minimize hydrophobic mismatch, as in the

https://doi.org/10.1038/s41589-025-02032-w

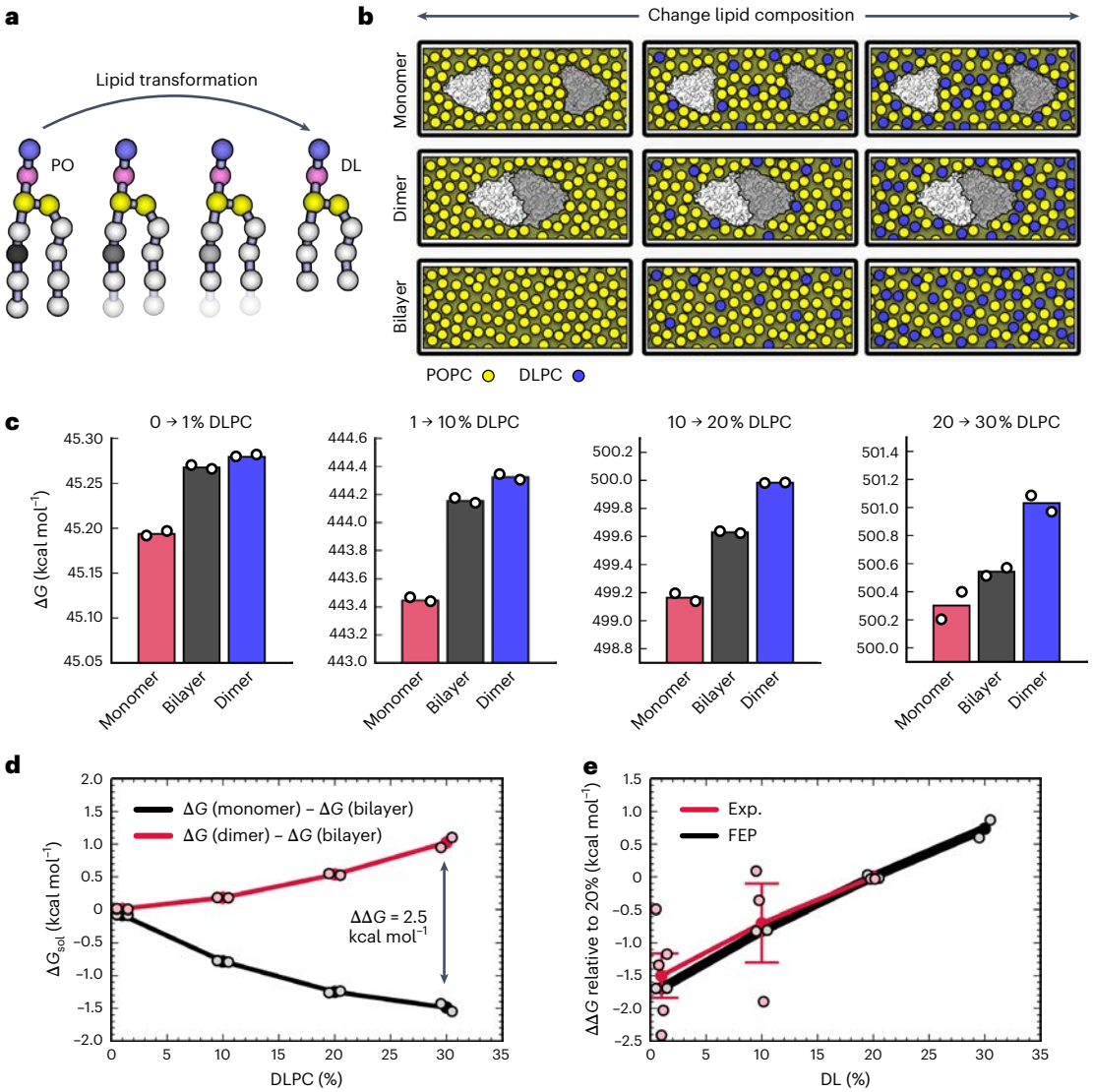

Fig. 5 | Calculation of free energy from a change in membrane composition, coupled to the CLC-ec1 dimerization. a, Schematic showing the alchemical transformation of a single CG POPC lipid to DLPC, by gradually turning off the parameters for the fourth bead on each chain (C4B) while simultaneously removing the double bond (D2A, black bead) by changing the bead type (C3 to C1). **b**, POPC lipid molecules are selected at random from the total lipid population and transformed into DLPC through small, step-wise increments for the dissociated monomers, dimer and a protein-free bilayer. **c**, The free energy cost of each transformation (ΔG) is calculated as the mean over the forward and backward paths (scatter dots, $n = 2$ technical replicates) for the dissociated monomers, dimer and membrane free lipid bilayer systems. **d**, The mean solvation free energy compares the change in free energies in the associated and dissociated states to the protein-free transformation. **e**, Comparison of $\Delta\Delta G$ as determined from FEP simulations in POPC/DLPC membranes and single-molecule photobleaching experiments carried out in POPE/POPG/DLPE/DLPG membranes[25]. Changes are reported relative to the free energy of each system in 20% DL lipids, where there are enough DL lipids to minimize system size artifacts (Extended Data Fig. 5a). For the experimental results, data represent mean ± s.e.m. for 1% and 10% DL, with $n = 5$ and $n = 3$ biological replicates, respectively. For 20% DL, $n = 2$, and so the data is shown as the average and individual scatter points. For the FEP, data represent mean from $n = 2$ forward and backward calculations. Individual data points shown in scatter. Exp., experiment.

case of model membrane proteins[44], gramicidin[45,46], transmembrane helices[47] and GPCRs[4]. As noted, this type of effect can be rationalized from a continuum mechanics perspective; that is, a geometrical mismatch represents a strain in the membrane energy, which can be minimized depending on the state of the protein. However, to understand how changes in lipid composition modulate this driving force, it is necessary to dive deeper into its molecular basis and directly examine and quantify differences in the spatial distribution of lipids around proteins as well as in the energetics of lipid solvation. This perspective is also supported by our recent experiments examining the thermodynamic changes associated with the CLC dimerization reaction[31]. This analysis showed that dimerization is accompanied by a large 2 kcal mol^{-1} K^{-1} change in heat capacity, that is, the thermodynamic signature of the hydrophobic effect[48–50]. Of course, the hydrophobic effect should not apply to these types of membrane protein reactions as there is little water in the membrane for the protein to be phobic of. However, when considered more broadly, the phenomenon arises from changes in solvent configurations and the degrees of freedom for heat to distribute across bonds and nonbonded interactions. In the CLC dimerization reaction, the solvent is primarily composed of lipids, and we observe major changes in lipid configurations between the monomer and dimer states. Therefore, the observation that this reaction exhibits the classic thermodynamic signature of the hydrophobic effect further supports our finding that the change in lipid-solvation energetics is a primary driving force for CLC dimerization.

A driving force that originates in the membrane is inherently dependent on the chemical composition of the lipids. This is where membrane protein reactions are remarkable to consider. For soluble

https://doi.org/10.1038/s41589-025-02032-w

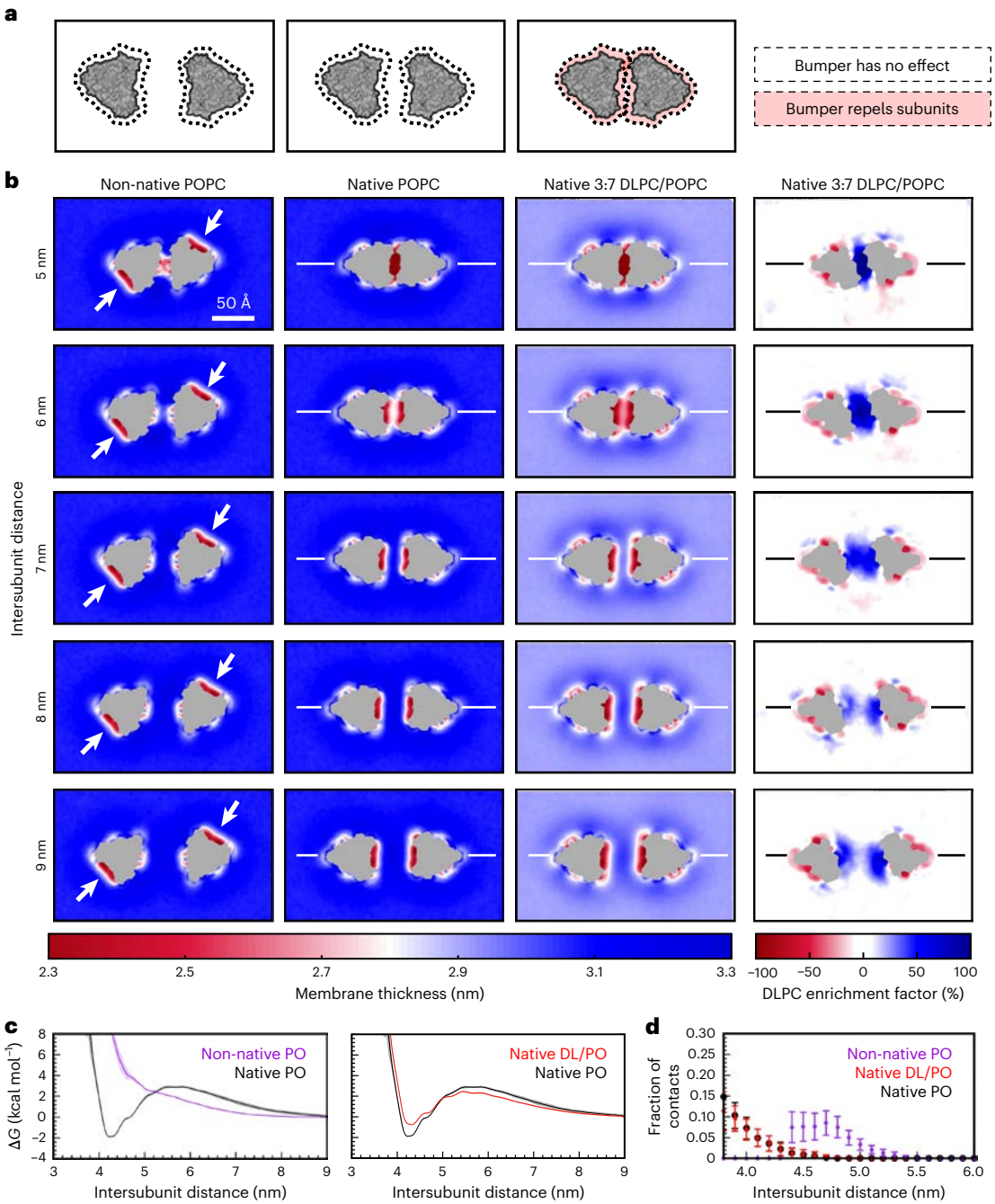

Fig. 6 | Burial of the membrane defect drives CLC-ec1 dimerization before protein contacts are made and provides specificity for the native orientation. From CGMD simulations using the MARTINI force field. **a**, To sample noncontact states, a bumper potential is imposed around the protein, providing a repulsive force when the distance separating individual subunit surfaces is <1.2 nm. For separating distances >1.2 nm, the bumper has no effect. **b**, Average membrane thickness maps (left) for non-native and native dimers in a POPC bilayer as a function of intersubunit separation distance. This distance is measured between the center of mass of a collection of beads located on each protomer (Extended Data Fig. 6), whereupon a separation of 3.4 nm is obtained in the native dimer complex, and 3.8 nm in the non-native state. The DLPC lipid enrichment factor is also shown in the outer leaflet (right). **c**, Free energy change as a function of intersubunit separation before protein contact formation, thereby isolating the membrane contribution for the non-native versus native dimer in POPC and native dimer complex in POPC versus a 70:30 mixture of POPC and DLPC. Data represent mean ± 3× s.d. around the mean obtained by splitting the trajectories into three nonoverlapping segments, and calculating the free energy from each segment, for $n = 3$ technical replicates. **d**, The fraction of interprotomer contacts, relative to those observed in the native dimer, as a function of intersubunit distance. Data represent the mean ± s.d. over all contacts for all snapshots and windows after sorting based on the intersubunit separation distance. Each bin contained approximately 40,000 samples for the native and non-native dimer in POPC and 120,000 samples for the DLPC/POPC mixture.

proteins, there is only one solvent available, that is, water. In contrast, cellular membranes exhibit nearly infinite possibilities of chemical variability. Our findings demonstrate that small changes in lipid composition can have a substantial impact on protein conformational equilibria. As changes in solvation energetics drive CLC dimerization, altering the lipid composition changes the driving force by modifying the solvation free energy of either state. Knowing how a certain lipid changes this balance is far from trivial, but the FEP approach we present provides a direct means of calculating lipid effects. Indeed, we find that increasing DL by 20% in the membrane changes both monomer and dimer solvation

free energies for a net difference of about 2.5 kcal mol^{-1}, consistent with our experimental measurements[25]. These calculations demonstrate that linkage of lipids to protein equilibria is complex, involving unique dependencies of each state and the reference lipid bilayer. Yet, this study demonstrates that quantitative modeling of lipid regulation is possible, providing self-consistent evidence between thermodynamic computations and experimental measurements. This methodology can be readily applied to many other types of systems where lipids are predicted to be linked to conformational equilibria, such as the activation and organization of GPCRs and other membrane proteins[51,52].

It is important to note that although we observe enrichment of DL lipids at the CLC dimerization interface, the inhibitory mechanism we uncover does not require specific sites on the protein for lipid binding. To the contrary, this enrichment effect entails a constant turnover of all lipids in the first lipid-solvation shells. Turnover rates are, however, lipid-specific, resulting in a tunable mechanism that produces substantial changes in dimerization energetics with small changes in lipid composition, with substantial implications for the regulation of membrane protein complexes in cellular membranes. A 2.5 kcal mol^{-1} change in dimerization stability corresponds to a change in the dissociation constant of about 70-fold (Extended Data Fig. 5b). If the protein expression levels are within the transition region of the dimerization isotherm, then this may decrease the dimer population by up to 60%. This sets up a potential mechanism for functional lipid regulation through modulation of dimerization. Although CLC-ec1 can function as both monomers and dimers, at the inactivating condition of pH 7.5, the prevalence of dimers increases[53], suggesting that inhibition might be linked to a particular dimer conformation that prevents transport activity. Our finding that DL lipids destabilize dimerization, and that DLPC specifically enhances the activity of the transporter (Fig. 2d,e), may reflect lipid-mediated regulation of CLC inhibition that could also pertain to biological settings. As noted, none of this requires individual DL lipids to become immobilized at the dimerization interface, in agreement with our previous linkage data showing that the inhibitory effect of DL does not saturate, as would be expected for site-specific, competitive binding. Indeed, alternatives to the lipid-ligand model of membrane regulation are increasingly compelling, as has been noted for other systems such as mechanosensitive channels[37]. We anticipate that future experimental and computational studies on the thermodynamic linkage between protein conformational equilibria and membrane composition will reveal that preferential lipid solvation is a ubiquitous mechanism by which lipids regulate membrane proteins.

Online content

Any methods, additional references, Nature Portfolio reporting summaries, source data, extended data, supplementary information, acknowledgements, peer review information; details of author contributions and competing interests; and statements of data and code availability are available at https://doi.org/10.1038/s41589-025-02032-w.

References

1. Ernst, M. & Robertson, J. L. The role of the membrane in transporter folding and activity. *J. Mol. Biol.* **433**, 167103 (2021).
2. Levental, I. & Lyman, E. Regulation of membrane protein structure and function by their lipid nano-environment. *Nat. Rev. Mol. Cell Biol.* **24**, 107–122 (2023).
3. Valiyaveetil, F. I., Zhou, Y. & MacKinnon, R. Lipids in the structure, folding, and function of the Kcsa K^+ channel. *Biochemistry* **41**, 10771–10777 (2002).
4. Botelho, A. V., Huber, T., Sakmar, T. P. & Brown, M. F. Curvature and hydrophobic forces drive oligomerization and modulate activity of rhodopsin in membranes. *Biophys. J.* **91**, 4464–4477 (2006).
5. Powl, A. M., East, J. M. & Lee, A. G. Anionic phospholipids affect the rate and extent of flux through the mechanosensitive channel of large conductance MscL. *Biochemistry* **47**, 4317–4328 (2008).
6. Sun, D. et al. Molecular mechanism for gramicidin dimerization and dissociation in bilayers of different thickness. *Biophys. J.* **117**, 1831–1844 (2019).
7. Argudo, D., Bethel, N. P., Marcoline, F. V. & Grabe, M. Continuum descriptions of membranes and their interaction with proteins: towards chemically accurate models. *Biochim. Biophys. Acta* **1858**, 1619–1634 (2016).
8. Ernst, R., Ejsing, C. S. & Antonny, B. Homeoviscous adaptation and the regulation of membrane lipids. *J. Mol. Biol.* **428**, 4776–4791 (2016).
9. Veatch, S. L., Rogers, N., Decker, A. & Shelby, S. A. The plasma membrane as an adaptable fluid mosaic. *Biochim. Biophys. Acta* **1865**, 184114 (2023).
10. Corradi, V. et al. Lipid–protein interactions are unique fingerprints for membrane proteins. *ACS Cent. Sci.* **4**, 709–717 (2018).
11. Reynwar, B. J. & Deserno, M. Membrane composition-mediated protein–protein interactions. *Biointerphases* **3**, FA117 (2008).
12. Beaven, A. H. et al. Gramicidin a channel formation induces local lipid redistribution I: experiment and simulation. *Biophys. J.* **112**, 1185–1197 (2017).
13. Sodt, A. J., Beaven, A. H., Andersen, O. S., Im, W. & Pastor, R. W. Gramicidin A channel formation induces local lipid redistribution II: a 3D continuum elastic model. *Biophys. J.* **112**, 1198–1213 (2017).
14. Fiorin, G., Marinelli, F. & Faraldo-Gómez, J. D. Direct derivation of free energies of membrane deformation and other solvent density variations from enhanced sampling molecular dynamics. *J. Comput. Chem.* **41**, 449–459 (2019).
15. Varma, M. & Deserno, M. The interplay of composition and mechanics in the thermodynamics of asymmetric ternary lipid membranes. *Faraday Discuss.* **259**, 200–233 (2025).
16. Laganowsky, A. et al. Membrane proteins bind lipids selectively to modulate their structure and function. *Nature* **510**, 172–175 (2014).
17. Gupta, K. et al. The role of interfacial lipids in stabilizing membrane protein oligomers. *Nature* **541**, 421–424 (2017).
18. Camara-Artigas, A., Brune, D. & Allen, J. P. Interactions between lipids and bacterial reaction centers determined by protein crystallography. *Proc. Natl Acad. Sci. USA* **99**, 11055–11060 (2002).
19. Dang, S. et al. Structural insight into TRPV5 channel function and modulation. *Proc. Natl Acad. Sci. USA* **116**, 8869–8878 (2019).
20. Baker, M. R. et al. Cryo-EM structure of type 1 IP3R channel in a lipid bilayer. *Commun. Biol.* **4**, 625 (2021).
21. Neuberger, A., Nadezhdin, K. D. & Sobolevsky, A. I. Structural mechanisms of TRPV6 inhibition by ruthenium red and econazole. *Nat. Commun.* **12**, 6284 (2021).
22. Zhang, Y. et al. Visualization of the mechanosensitive ion channel MscS under membrane tension. *Nature* **590**, 509–514 (2021).
23. Stanley, A. M. & Fleming, K. G. The transmembrane domains of ErbB receptors do not dimerize strongly in micelles. *J. Mol. Biol.* **347**, 759–772 (2005).
24. Marsh, D. Preferential solvation and the selectivity of lipid-protein interactions. *Biophys. J.* **69**, 1191–1192 (1995).
25. Chadda, R. et al. Membrane transporter dimerization driven by differential lipid solvation energetics of dissociated and associated states. *eLife* **10**, e63288 (2021).
26. Wyman, J. & Gill, S. J. *Binding and Linkage: Functional Chemistry of Biological Macromolecules* (University Science Books, 1990).
27. Jarmoskaite, I., AlSadhan, I., Vaidyanathan, P. P. & Herschlag, D. How to measure and evaluate binding affinities. *eLife* **9**, e57264 (2020).
28. Maduke, M., Pheasant, D. J. & Miller, C. High-level expression, functional reconstitution, and quaternary structure of a prokaryotic ClC-type chloride channel. *J. Gen. Physiol.* **114**, 713–722 (1999).

29. Dutzler, R., Campbell, E. B., Cadene, M., Chait, B. T. & MacKinnon, R. X-ray structure of a ClC chloride channel at 3.0 Å reveals the molecular basis of anion selectivity. *Nature* **415**, 287–294 (2002).
30. Chadda, R. et al. The dimerization equilibrium of a ClC Cl^-/H^+ antiporter in lipid bilayers. *eLife* **5**, e17438 (2016).
31. Chadda, R. et al. A thermodynamic analysis of CLC transporter dimerization in lipid bilayers. *Proc. Natl Acad. Sci. USA* **120**, e2305100120 (2023).
32. Ernst, M., Orabi, E. A., Stockbridge, R. B., Faraldo-Gómez, J. D. & Robertson, J. L. Dimerization mechanism of an inverted-topology ion channel in membranes. *Proc. Natl Acad. Sci. USA* **120**, e2308454120 (2023).
33. Anselmi, C., Davies, K. M. & Faraldo-Gómez, J. D. Mitochondrial ATP synthase dimers spontaneously associate due to a long-range membrane-induced force. *J. Gen. Physiol.* **150**, 763–770 (2018).
34. Guardia, C. M. et al. Structure of human ATG9A, the only transmembrane protein of the core autophagy machinery. *Cell Rep.* **31**, 107837 (2020).
35. Chadda, R. & Robertson, J. L. Measuring membrane protein dimerization equilibrium in lipid bilayers by single-molecule fluorescence microscopy. *Methods Enzymol.* **581**, 53–82 (2016).
36. Cliff, L., Chadda, R. & Robertson, J. L. Occupancy distributions of membrane proteins in heterogeneous liposome populations. *Biochim. Biophys. Acta Biomembr.* **1862**, 183033 (2019).
37. Park, Y. C., Reddy, B., Bavi, N., Perozo, E. & Faraldo-Gómez, J. D. State-specific morphological deformations of the lipid bilayer explain mechanosensitive gating of MscS ion channels. *eLife* **12**, e81445 (2023).
38. Bernhardt, N. & Faraldo-Gómez, J. D. MOSAICS: a software suite for analysis of membrane structure and dynamics in simulated trajectories. *Biophys. J.* **122**, 2023–2040 (2023).
39. Rouviere, E., Arnarez, C., Yang, L. & Lyman, E. Identification of two new cholesterol interaction sites on the A2A adenosine receptor. *Biophys. J.* **113**, 2415–2424 (2017).
40. Shirts, M. R. & Mobley, D. L. An introduction to best practices in free energy calculations. *Methods Mol. Biol.* **924**, 271–311 (2012).
41. Liu, J. & Gumbart, J. C. Membrane thinning and lateral gating are consistent features of BamA across multiple species. *PLoS Comput. Biol.* **16**, e1008355 (2020).
42. Pleiner, T. et al. Structural basis for membrane insertion by the human ER membrane protein complex. *Science* **369**, 433–436 (2020).
43. McDowell, M. A. et al. The GET insertase exhibits conformational plasticity and induces membrane thinning. *Nat. Commun.* **14**, 7355 (2023).
44. Lagüe, P., Zuckermann, M. J. & Roux, B. Protein inclusion in lipid membranes: a theory based on the hypernetted chain integral equation. *Faraday Discuss.* **111**, 165–172 (1999).
45. Goodall, M. C. Thickness dependence in the action of gramicidin A on lipid bilayers. *Arch. Biochem. Biophys.* **147**, 129–135 (1971).
46. Goforth, R. L. et al. Hydrophobic coupling of lipid bilayer energetics to channel function. *J. Gen. Physiol.* **121**, 477–493 (2003).
47. Yano, Y. & Matsuzaki, K. Measurement of thermodynamic parameters for hydrophobic mismatch 1: self-association of a transmembrane helix. *Biochemistry* **45**, 3370–3378 (2006).
48. Baldwin, R. L. Temperature dependence of the hydrophobic interaction in protein folding. *Proc. Natl Acad. Sci. USA* **83**, 8069–8072 (1986).
49. Privalov, P. L. & Gill, S. J. Stability of protein structure and hydrophobic interaction. *Adv. Protein Chem.* **39**, 191–234 (1988).
50. Clapham, D. E. & Miller, C. A thermodynamic framework for understanding temperature sensing by transient receptor potential (TRP) channels. *Proc. Natl Acad. Sci. USA* **108**, 19492–19497 (2011).
51. Mondal, S. et al. Membrane driven spatial organization of GPCRs. *Sci. Rep.* **3**, 2909 (2013).
52. Leonard, A. N. & Lyman, E. Activation of G-protein-coupled receptors is thermodynamically linked to lipid solvation. *Biophys. J.* **120**, 1777–1787 (2021).
53. Fortea, E. et al. Structural basis of pH-dependent activation in a CLC transporter. *Nat. Struct. Mol. Biol.* **31**, 644–656 (2024).

Methods

Visualization of lipid orientations around CLC monomers and dimers from CGMD simulations

A depiction of lipid orientations around CLC-ec1 is provided in Fig. 1 calculated from CGMD MARTINI 2:1 POPE/POPG simulation data acquired in a previous study[25]. Time-average lipid coordinates were computed using the trajectory data and 'Mean Lipid Coords' tool provided in MOSAICS[38]. In this case, the lipids are mapped onto a grid using a stamping radius of 2.3 Å and a lattice spacing of 4 Å. The resulting coordinates, which are provided for each CG bead and at every lattice point, are visualized as arrows connecting the phosphate bead and the last bead on chain A. Therefore, arrows represent the average orientation when a lipid is at a lattice point at a user-defined lattice spacing and do not reflect the actual lipid packing density in the membrane. Due to the isotropic nature of the lipids, the average coordinates of beads on chain A are identical to those on chain B. In Fig. 1, a surface is also shown around the protein for reference, where the coordinates are also averaged over the trajectory, and only a single layer of lattice points surrounding the protein is shown for clarity.

CLC-ec1 purification, fluorophore labeling and reconstitution into lipid bilayers

The protein was purified, labeled and reconstituted following established methods[25,30]. CLC-ec1 on the background of C85A/H234C was used in the studies to provide subunit-specific labeling. A C-terminal hexahistidine tag is present for purification and is left intact in these studies. Protein was labeled with Cy5-maleimide (sulfo-Cy5, GE Biosciences), with a labeling efficiency of ≈0.7 per subunit. CLC-ec1-Cy5 was reconstituted into POPC or 1:4 DLPC/POPC membranes[30], where dialysis was carried out at 4 °C for ~3 days, unless otherwise noted. Chloride transport activity was measured using the ion electrode-based chloride dump assay[54], where transport was quantified by measuring the initial rate (k_{init}) through linear fitting of the first 10 s of transport following addition of valinomycin/carbonyl cyanide-p-trifluoromethoxyphenylhydrazone (FCCP). A biological replicate is defined as an independent sample that has been separately purified, labeled and reconstituted.

Freeze-thaw fusion of membranes

Fusion of 2:1 POPE/POPG, POPC and 1:4 DLPC/POPC membranes was monitored by Förster Resonance Energy Transfer in membranes (Extended Data Fig. 1c,d) detected by doping vesicles with 0.02% donor 18:1PE-NBD (1,2-dioleoyl-sn-glycero-3-phos-phoethanolamine-N-(7-nitro-2-1,3-benzoxadiazol-4-yl)), 0.1% acceptor 18:1 PE-RhB (1,2-dioleoyl-sn-glycero-3-phosphoethanolamine-N-(lissa-mine rhodamine B sulfonyl)) or both following the procedures described previously[36]. Measurements were conducted using a Fluorolog 3–22 Fluorometer (Horiba). The ratiometric FRET signal is normalized between the negative control baseline FRET signal of the 0.02% NBD and 0.1% RhB combined samples before fusion (set to 0) and the positive control endpoint signal from the 0.02% NBD/0.1% RhB co-labeled proteoliposomes samples (set to 1.0).

Single-molecule photobleaching analysis

After dialysis, liposomes were freeze-thawed five times by cycling through −80 °C and room temperature. The fused membranes were then supplemented with 0.02% NaN_3 and incubated at room temperature, in the dark, for 4–8 days. The samples were extruded through a 0.4 µm Avestin extruder 21x before examination by single-molecule total internal reflection fluorescence microscopy. Lanes on the slide were coated with 1 mg ml^{-1} polylysine and dilute glutaraldehyde to immobilize protein molecules and reduce lateral diffusion. Photobleaching probability distributions were measured and analyzed as described previously[30,35].

All-atom MD simulations

Starting CLC-ec1 configurations are taken from the Protein Data Bank (PDB) entry 1OTS[55]. A single protomer is extracted for simulation and the first 30 residues are removed since these were shown in a previous study to be highly flexible and adopt multiple conformations[56]. Following truncation, the N and C termini are capped with acetyl and methylamine groups, respectively, and E113 (chain A and B) and D417 (chain A) were protonated, and all other residues were left in default protonation states (GLU^{-1}/ASP^{-1}, LYS^{+1}/ARG^{+1}, HIS^{0}) in line with previous continuum electrostatics calculations predicting pKa states[57]. The protein was inserted into a pre-equilibrated lipid bilayer using the GRIFFIN tool[58]. The system is then buffered using a TIP3P water model, 150 mM NaCl ions and the net charge neutralized (see Supplementary Table 5 for details on molecular composition). Initial equilibrations of the systems are performed using NAMD 2.12 (ref. 59) in a multistaged protocol where structural restraints are gradually reduced over approximately 100 ns of simulation time (Supplementary Table 6). Production runs are then performed using the Anton 2 special computing cluster[60] and the CHARMM36m force field[61]. For these simulations, the equations of motion are integrated with the Anton Multigrator scheme[62] using a timestep of 2.5 fs. Likewise, the temperature and pressure are both maintained at 310 K and 1 bar, respectively, using a Langevin thermostat and a semi-isotropic Nose-Hoover barostat.

In some cases, cumulative force field inaccuracies can lead to deviations where important secondary and tertiary structural elements can be degraded after multiple microseconds of simulation time. Therefore, we introduce a term that biases the configurational sampling of backbone dihedral angles to favor a selected set of reference values, specifically those observed in the crystal structure (PDB ID: 1OTS). These terms do not preclude deviations of individual dihedral angles, as local structural fluctuations are allowed and are observed in the simulations. Yet collectively, large-scale structural changes are avoided since the bias limits the accumulation of many angles changing all at once. These restraints have been used in previous simulations on Anton 2 (refs. 37,63,64) and target the protein's phi and psi angles using the following energy function:

$$U(\phi_t) = K\sum_{m=1}^{m=6}(-1)^m\left(\frac{1+\cos\left(m\left(\phi_t-(\phi_{\exp}-180)\right)\right)}{m!}\right) \quad (1)$$

where ϕ_t is the angle computed at time t, $\phi_{\exp}$ is the reference angle taken from the experimental structure, and K is the force constant chosen to be 1 k_BT in our simulations, where k_B is the Boltzmann constant and T is the temperature. Select contacts at the binding interface are also enforced using harmonic restraints (Supplementary Table 7) to ensure maximal integrity of the dimerization interface.

Noise-corrected projections of the lipid residence time

Projections of the time average lipid residence time are made with the MOSAICS v1.1.0 toolset (https://github.com/MOSAICS-NIH/MOSAICS) by computing Voronoi tessellations of the trajectory snapshots[38]. MOSAICS approximates Voronoi cells using a grid-based method that assigns lattice points to lipids that are closer to the lattice point than any other lipid. The method uses the lipid's carbonyl carbons to define the vertices and has been shown to produce accurate tessellations in area per lipid calculations, provided the lattice spacing is small. Here we use a grid-point spacing of 0.7 Å, which is sufficient for mapping the lipid dwell time. We note that the dwell time estimates computed from tessellation data are subject to noise caused by internal fluctuations of the lipid atoms. For example, the Voronoi cell of a bound lipid molecule may appear to pop in and out of a binding pocket due to the motions of the lipid's ester groups, which as noted are used to construct the Voronoi cells. In this case, the lipid will appear to bind to the protein multiple times, and the average dwell time underestimated. This problem is circumvented by consolidating the fragmented binding

events into a single event. However, care must be taken to ensure that uncorrelated events are not included in the merge. This is accomplished by limiting the gap size between neighboring events that are mended to the timescale describing the lipid's internal motions. The resulting gap size is determined from analysis of the lipid molecules' mean square displacement (MSD) after an elapsed time τ. Figure 3b shows a plot of the MSD versus τ where the diffusion equation describes the linear region. Before this region, the lipid displacement deviates from the diffusion equation because the internal motions now account for a large portion of the overall movement. Still, the probability of a true lipid displacement event is negligible for this small timescale and only becomes significant when larger durations that exceed 50 ns are considered. We, therefore, minimize noise in dwell time estimates by merging all binding events that originate from a single lipid molecule and that are separated by no more than 50 ns.

Computation of residence time in, and lipid exchange probabilities between, solvation shells

Characterizations of the lipid dynamics in the protein's solvation shells are made using the 'Solvation Shells' tool of MOSAICS[38]. This tool assigns the lipid molecules, represented in Voronoi tessellation data, to a solvation shell based on the lipid's neighbors. These assignments are made using the following set of heuristics:

1. If the lipid shares a border with the protein, it is a first shell lipid.
2. If the lipid is not a first shell lipid but shares a border with one, then it is a second shell lipid.
3. If the lipid is not a first or second shell lipid but shares a border with one, then it is a third shell lipid.

Following these rules, bordering lipids are determined by measuring the shortest distance between Voronoi cells and requiring this distance be within 3 Å. Lipids are then assigned a solvation shell number for each trajectory snapshot (Fig. 4b). Given this approach, the shell assignments will be susceptible to the same errors encountered when computing spatially resolved mean residence times. Namely, the internal vibrations of the lipid molecules lead to spurious transitions between shells that should be ignored in any serious analysis of the lipid dynamics. We thus perform noise filtering of the shell assignments with a width of 50 ns as determined by the time needed to observe lipid-lipid displacement events that initiate diffusion. In this case, the filtered shell number assumes the value most frequently observed within the window. The resulting shell assignments can be seen in Fig. 4b and Supplementary Video 2, and these assignments are used when reporting the number of lipids solvating each interface (Extended Data Fig. 2d,e).

With the lipid molecules sorted into shells, the dynamics in the first two shells are characterized. Specifically, we compute the lipid dwell time in each shell, as well as the probability that DLPC enters one of the shells when exchanges occur with that shell's next neighbor. For example, the first shell exchanges with the second shell, and the second shell exchanges with the third. For lipid exchanges, we select pairs of lipids using a criterion designed to detect both direct and indirect exchanges. A direct exchange is defined as one in which the incoming lipid populates the same space previously occupied by the outgoing lipid. In contrast, indirect exchanges occur when the outgoing transition is accompanied by lateral movement along the protein interface by the remaining lipids in the same shell. In this latter case, the incoming lipid can enter the shell at a separate location, ultimately occupying a space within the shell that is distinct from where the outgoing lipid was positioned. To detect both cases, we select exchange partners to minimize the time separating when one lipid leaves the solvation shell and when the other enters.

Applying this approach, we find that lipid swaps are typically fast, occurring within 10 ns or less (Extended Data Fig. 2f), and that both direct and indirect exchanges are common. To distinguish between each type, we compute the distance separating exchange partners, or more precisely, the space occupied by each partner when it is in the solvation shell of interest. Exchanges occur over a range of distances, with many partners populating the same space and others residing in regions that are several nanometers apart (Extended Data Fig. 2g). We note that the exchange distances are extended for the nondimerization interface, as evident from the emergence of a peak centered at 6 nm. This peak corresponds to 40% of the sampled exchanges and represents events where the two lipids solvate different faces on the nondimerization interface (Extended Data Fig. 2h). These exchanges are not correlated and are removed from the analysis by splitting the nondimerization interface into two equally sized sections, ND1 and ND2, with each having about 15 lipids on average (Extended Data Fig. 2d). The analysis is then performed on each section separately, thereby reducing the number of uncorrelated events substantially.

With the exchange partners identified, we group them by the leaving lipid type and compute the probability that the incoming lipid is DL (Fig. 4i and Extended Data Fig. 2i). We then compute the probability that DL enters the first shell given that PO leaves or the probability that DL enters when DL leaves. We note that the probability that PO enters the same shell, given a specific leaving type, is computed as one minus the corresponding probability for DL (Extended Data Fig. 2j). The expected random exchange probability corresponds to the bulk lipid mole fraction, that is, 0.3 for DLPC or 0.7 for POPC. The difference between these bulk concentrations and the observed exchange probability thus highlights the exchange preferences in the solvation shells around the protein (Fig. 4i and Extended Data Fig. 2i).

Error estimates are reported for these quantities by splitting the trajectory into three equally sized segments and computing averages over each. The s.e.m. is then computed as:

$$\text{s.e.m.}_x = \sqrt{\frac{\sigma_x^2}{n}} \tag{2}$$

where n is the number of measurements, in this case three, and σ_x is their s.d.

Calculations of diffusion coefficients

Diffusion coefficients (D) are computed for each lipid species using the Einstein relation:

$$\left\langle \left(\vec{r} - \vec{r}_0\right)^2 \right\rangle = 2nD\tau \tag{3}$$

where $n = 2$ and is the dimensionality in which diffusion occurs, τ is the elapsed time, and $\langle(\vec{r} - \vec{r}_0)^2\rangle$ is the MSD; $\vec{r}_0$ is then a position vector computed for the lipid's geometric center and $\vec{r}$ is this vector after τ. Of note, we only use heavy atoms, that is, excluding hydrogen atoms, when computing r and $\vec{r}_0$. Moreover, to make the most of our data, we let the initial time, from which we take $\vec{r}_0$, vary. Likewise, the MSD for each timepoint is averaged over the individual lipids. Before any calculations, the molecular system is unwrapped to remove periodic boundary effects. This step is performed using the PBC XY tool of MOSAICS, which accounts for fluctuations in volume that, if not removed, lead to exaggerated motions of the lipid molecules[65].

Estimations of the DLPC lipid enrichment factor from exchange rates and lipid dwell times

Here we develop a relationship between the lipid's mean residence time, their exchange probability, and the DLPC lipid enrichment factor. The DLPC enrichment factor is defined as:

$$\%E = \frac{1}{R}\left(\left(\frac{\rho_{\text{DL}}}{\rho_{\text{PO}}}\right) - R\right)100\% \tag{4}$$

where ρ is the lipid density for either DLPC or POPC as indicated by the subscript and R is the corresponding ratio in the bulk, that is,

$R = [\frac{\rho_{DL}}{\rho_{PO}}]_B = \frac{30}{70}$. In practice, ρ is computed as the total amount of time the lipids of the desired type are present. This can be computed as:

$$\rho = n_{\text{lipid-visit}} \times \bar{t} \tag{5}$$

where $n_{\text{lipid-visit}}$ is the total number of times the lipid visits the interface and $\bar{t}$ is the average dwell time. Moreover, $n_{\text{lipid-visit}}$ is related to the lipid exchange probability by:

$$n_{\text{lipid-visit}} \approx n_{\text{lipid-exchange}} \times P \tag{6}$$

where $n_{\text{lipid-exchange}}$ is the total number of lipid exchanges and P is the exchange probability. Plugging these results into our expression for enrichment, we get the desired result:

$$\%E = \frac{1}{R}\left(\frac{P_{DL} * \bar{t}_{DL}}{P_{PO} * \bar{t}_{PO}} - R\right)100\% \tag{7}$$

Branching from equation (7), we can gauge the effects of the dwell times or exchange probabilities separately. For example, if we assume the average dwell time for POPC and DLPC is equal, then equation (7) simplifies to:

$$\%E = \frac{1}{R}\left(\frac{P_{DL}}{P_{PO}} - R\right)100\% \tag{8}$$

Similarly, if we assume each exchange probability to be equal to the corresponding lipid concentration, then we get:

$$\%E = \left(\frac{\bar{t}_{DL}}{\bar{t}_{PO}} - 1\right)100\% \tag{9}$$

Equations (7)–(9) are used to estimate the overall and individual contributions to the DLPC enrichment factor from kinetics data. Estimates of each are provided for the first two solvation shells in Supplementary Table 4, where s.e.m. is computed by splitting the trajectory into three parts ($n = 3$) and analyzing each separately.

Contact analysis

Ordinary contacts between the protein and lipids are counted using a distance cutoff of 3.5 Å. These contacts were measured between the protein and lipids while including the full set of atoms from each. For counting the number of hydrogen bonds, we use a convention that considers the angle between the donor, acceptor, and hydrogen atoms, as well as the distance between the donor and acceptor atoms. Hydrogen bonds thus require the angle to be less than 30° and the distance below 3.5 Å (Extended Data Fig. 3a). Donor atom types on the protein include the backbone and side-chain nitrogen and oxygens. Since POPC and DLPC molecules contain only acceptor atoms, that being the carbonyl and phosphate oxygens, no acceptor types are required for the protein. Salt bridges are then counted as select hydrogen bonds between the lipid and charged amino acids Lys, Arg and His (Extended Data Fig. 3b). Salt bridges between choline and charged residues Glu and Asp are weak and rarely formed (Extended Data Fig. 3c) and are excluded in the main analysis (Fig. 4f).

Calculation of free-energy changes from variations in lipid composition

Considering the lipid dynamics observed in our all-atom MD simulations of monomeric CLC-ec1, we seek to demonstrate that the redistribution effects indeed explain the shift in the monomer-dimer equilibrium constant that is experimentally measured upon addition of DL lipids to PO membranes. To establish this interpretation based on simulation data, we must calculate the change in the free energy of dimerization when the lipid composition of the membrane is altered and compare the result with experimental data. In principle, this problem can be approached in the following two ways: a calculation might be designed to simulate the association and dissociation of CLC-ec1 monomers, in different membrane conditions, deducing the dimerization free-energy in each case; or alternatively, a series of simulations might be designed to calculate, separately for the dimer and dissociated monomers, the free-energy gain or loss upon a change in the lipid composition of the membrane, deriving from the results the change in dimerization free-energy (Fig. 5b). While the first approach seems more intuitive, it is also more prone to error, as the mechanism of monomer–monomer recognition is unknown at the molecular level. Thus, we follow the second approach; to do so, we adapt a simulation methodology designed to evaluate differentials in solvation energetics for small molecules, known as FEP[40].

Here we use this 'alchemical' approach to transform not one solute, but the total composition of the lipid bilayer solvent. To do so, we gradually morph randomly-selected POPC lipids into DLPC, for both the dissociated and associated states of CLC-ec1, as well as for a protein-free membrane, which we use as a reference. Convergence of the calculated free energy changes requires extensive sampling; therefore, we purposely carried out these calculations using CGMD simulations and the MARTINI force field to facilitate this. Since the ultimate transition from 0 → 30 % DLPC involves hundreds of molecules, we split the computation into multiple segments such that DLPC lipids are gradually added to the system (Supplementary Table 8), which also allows comparison with the experimental titration curves. Four transformation steps are carried out, starting with 0 → 1%, 1 → 10%, 10 → 20%, and finally 20 → 30% DLPC. Of course, the FEP methodology is built on the assumption that the phase space dimensions are unaffected by a given transformation, that is, the number of atoms does not change. In cases where one or more atoms are deleted, this limitation is circumvented by introducing dummy atoms, whose through space interactions are muted (that is, set to zero). For our simulations, we create a modified DLPC molecule, referred to as DLPC*, that is identical to the original DLPC but with a dummy atom attached to the end of each alkyl chain. These added beads are given standard bonding and angle bending parameters (Supplementary Table 9), and their Lennard-Jones terms are set to nil. MD simulations containing DLPC* are indistinguishable to those containing DLPC, as indicated by established metrics like membrane thickness and leaflet interdigitation (Extended Data Fig. 7). Notably, the dummy molecules preserve the spatial distribution of the lipids, as can be seen by examination of the DLPC enrichment factor.

Given that DLPC* and DLPC are indistinguishable, we transform POPC molecules into DLPC* in our FEP simulations by transforming chain length, saturation and energy parameters (Fig. 5a). These simulations are carried out using Hamiltonian replica exchange[66] where the scaling parameter λ is varied for each replica, thus improving sampling. To enable error estimates, we perform two independent simulations for each transformation, capturing the forward and backward paths. That is, we perform the following two simulations: one where λ is varied from 0 to 1 as we move across the replicas, and another where this distribution is reversed. The estimated free energy cost for each transformation as a function of simulation time is obtained using the GROMACS implementation of the Bennett acceptance ratio[67] (Extended Data Fig. 8a,b). We note that these distributions are slow to converge, requiring 6 µs for the 1 → 10%, 10 → 20%, and 20 → 30% transformations and 40 µs for the 0 → 1% condition. In the case of the 20 → 30% transformation, it is evident that the systems are approaching convergence, although not entirely there compared to the other transformations. Still, when the uncertainty in these computations is propagated into the solvation free energy calculations (Fig. 5c–e), the errors show that the quantities are sufficiently converged to not change the conclusions in a meaningful way.

FEP simulations are based on the CLC-ec1 constructs simulated in umbrella sampling simulations described next, specifically a dimer in both associated and dissociated states; an additional system is constructed that contains no protein for reference. In cases where a protein is present, starting structures are taken from initial steps of the

umbrella sampling simulations, that is, from the outside windows where the monomers are initially associated or separated by 5.5 nm. The protein is then converted into a CG model using the Martinize tool and the Martini 2.2 force field parameters[68]. The membrane and solvent use the Martini 2.0 force field[69] and are built around the protein, if present, using the INSANE script[70]. The net charge is neutralized, water is added and the system is buffered to 0.150 M with Na^+ and Cl^- ions. An energy minimization step is then performed, and the system is equilibrated at constant pressure and temperature for 10 ns. This results in a box with approximate dimensions 25.2 nm × 15.1 nm × 9.6 nm. The coordinates of this system are used to create the initial structure for each transformation by modifying select residue types in the topology file (see Supplementary Table 8 for details). Each system is then equilibrated for 1 µs at constant temperature and pressure, thereby randomizing the distribution of DLPC* molecules, which were selected in sequence. This equilibration step is followed by a slow growth simulation where the transformation is performed over the course of 20 µs. This, along with our FEP simulations, restricts the distance between monomers and the protein orientation, following the protocol used in umbrella sampling simulations. The FEP simulations are then carried out using Hamiltonian replica exchange such that λ is varied for each replica.

It is important to note that the free energy cost of carrying out the transformations is, in each case, hundreds of kilocalories per mole. Yet the important quantity, which is how the cost differs between the associated and dissociated states, is a small fraction of this ΔG (Extended Data Fig. 8a,b). The calculations described here are thus exceedingly challenging, as relatively small statistical errors in the calculated values can completely obscure the effect we seek to evaluate. Long sampling times and judicial design of the alchemical transformations are crucial to achieve complete mixing of all the lipid components and thus minimize these errors (Extended Data Fig. 4b). Our simulations thus use a set of λ values derived by restricting the relative entropy between neighboring replicas to a value of $1\,k_BT$ or less (Extended Data Fig. 8c). This requirement ensures substantial overlap between the probability distributions of neighboring replicas and results in 38 replicas for the 0 → 1% transformation and 93 for the remaining (Supplementary Table 10). These λ distributions are determined by performing a short simulation with uniform spacing and measuring the relative entropy between neighboring replicas. Since the λ spacing is uniform, each replica can be thought of as a bin spanning the λ space. These bins are then assigned a density proportional to the relative entropy. The λ space is then split into blocks, and the replicas are redistributed over each based on the density summed over the bins within the block. Like the initial trial, the replicas in each block are distributed with equal λ spacing. Tweaks are then made as needed, following another short simulation with this refined distribution. It is noted that the slow growth simulation described previously provides equilibrium structures for launching the trial simulations described here, as well as the FEP simulations with the optimized λ distribution. Production runs are then carried out with GROMACS 2018.8 (ref. 71) using an integration step of 20 fs and exchange moves between neighboring replicas are attempted every 1 ns. This results in an average exchange rate of approximately 40%. The pressure and temperature are set to 1 bar and 303 K using the semi-isotropic Berendsen barostat[72] along with the velocity-rescaling algorithm[73]. The electrostatics are treated with the reaction-field method. Trajectories are collected using 6 µs for each replica for the 1 → 10%, 10 → 20% and 20 → 30% DLPC conditions and 40 µs for the 0 → 1% condition. A total of 16.58 ms of simulation time is acquired.

Finally, it is worth noting that the molecular systems simulated here contain a lipid-to-protein ratio that is approximately 1,000 times smaller compared to the experimental conditions. Thus, to mimic the experimental degree of protein dilution, our simulation systems would have to be 1000 times larger, making the calculations unfeasible at the present time. The implication of this size discrepancy is that the number of DL lipids available to solvate each protein molecule is much greater under experimental conditions, and so the inhibitory effect of DL is necessarily more pronounced in experiment (Extended Data Fig. 5). To compare with simulation, therefore, we must factor out this size effect. A simple way to do so is to compare calculated and experimental free-energy values in reference to the largest DL molar fraction, that is the condition in which the DL enrichment is not limited by the number of DL lipids available, in either protein state; if we do this by comparing changes relative to the 20% DL condition, there is clear agreement between calculated and measured shifts in the dimerization free-energy (Fig. 5e).

Computations of the change in lipid solvation free energy, $\Delta\Delta G$

ΔG values are reported for each transformation as the average over the forward and backward paths such that:

$$\Delta G_{0\to1,x} = \frac{1}{2}\left(\Delta G_{0\to1,x,\mathrm{f}} + \Delta G_{0\to1,x,\mathrm{b}}\right) \tag{10}$$

where the subscripts f and b refer to the forward and backwards paths, whereas x is a placeholder for the associated state (a), dissociated state (d) or a membrane absent of any protein (m). Similarly, 0 → 1 indicates that the transformation is made from 0% to 1% DLPC. It then reasons that the free energy change taken over the full transformation, that is, from zero to thirty percent DLPC, is given as the sum of the individual steps:

$$\Delta G_{0\to30,x} = \Delta G_{0\to1,x} + \Delta G_{1\to10,x} + \Delta G_{10\to20,x} + \Delta G_{20\to30,x} \tag{11}$$

Using equation (11), the solvation energy is computed as:

$$\Delta G^{\mathrm{sol}}_{0\to30,\mathrm{a/d}} = \Delta G_{0\to30,\mathrm{a/d}} - \Delta G_{0\to30,m} \tag{12}$$

where the subscript a/d indicates the corresponding energy for the associated or dissociated state. Similarly, $\Delta\Delta G_{0\to30}$ is computed as:

$$\Delta\Delta G_{0\to30} = \Delta G_{0\to30,a} - \Delta G_{0\to30,d} \tag{13}$$

It is noted that, while the examples shown here focus on the complete transformation, the equations are easily adaptable to partial transformations, such as 0 → 1%, 0 → 10% or 0 → 20%. Moreover, we note that the s.e.m. is not computed for these free energies, as we only have two independent samples. However, we do include the individual data points in Fig. 5, as differences between the forward and backward paths quantify the simulation convergence. This property emerges since the free energy is a state function. Consequently, both paths should provide similar results within sampling variability.

Umbrella sampling simulations

The membrane's contribution to the association free energy of the CLC-ec1 dimer is computed using umbrella sampling simulations. These simulations span multiple states of the association reaction for three different molecular systems, including a native dimer in POPC, a non-native dimer in POPC, and a native dimer in a 3:7 mixture of DLPC and POPC. In each case, multiple copies of the molecular system, referred to as windows, are simulated, where a biasing potential is applied to target a specific intersubunit distance that varies for each window. These biasing potentials are used to improve sampling along the reaction coordinate, which is the intersubunit distance of the protomers, thus providing an improved estimate of the free energy profile that is recovered in postanalysis using methods like the weighted histogram analysis method[74]. Since extensive simulation time is required to ensure proper sampling of all windows, we use a CG representation of the molecular systems using the MARTINI force field in the current study.

The first two molecular systems are constructed by inserting CLC-ec1 dimers into a pre-equilibrated membrane patch containing pure POPC; the mixed membrane system is then considered. The initial membrane patch is constructed by placing POPC molecules inside a box

with dimensions 25 nm × 25 nm × 10 nm. Following this step, the bilayer is hydrated and buffered with 0.150 M NaCl. A simulation is then performed for 20 µs to allow the lipid molecules to redistribute away from their initial configuration. The equilibrated membrane patch is used to construct a series of CG models, each of which is used for a window in the first two umbrella sampling simulations. These models include a CLC-ec1 dimer whose protein orientation is varied, giving rise to a native and non-native dimer, where the dimerization interface of one protomer faces the other for the native dimer but not for the non-native (Extended Data Fig. 6a,b)[75]. Models for the native dimer are built using coordinates from the CLC-ec1 crystal structure (PDB ID: 1OTS)[55], while the non-native dimer is created using the HDOCK server[76]. In both cases, the protein is truncated, removing the first 30 residues since these were shown to be highly flexible in a previous study[56]. The protein is then converted to a CG representation using the Martinize script, and the protomers are translated along the x axis in increments of 0.05 nm to achieve an intersubunit distance ranging from 0.0 nm to 5.5 nm. These translations result in a total of 111 windows for both the native and non-native dimers.

Given the proper orientation and separating distance, each protomer is embedded into the pre-equilibrated membrane patch, and the resulting molecular system is subjected to a pair of energy minimization steps followed by a four-stage equilibration that restrains the backbone beads of the protein while the lipids equilibrate around the protein. Production runs are then performed, where each window is simulated for 10 µs. The production runs use the velocity-rescale algorithm[73] and the semi-isotropic Parrinello-Rahman barostat[77] to maintain the temperature and pressure of 310 K and 1 bar, respectively. Notably, our simulations introduce a restraint that maintains the distance between the protomers and a second that fixes each protomer's orientation relative to the other. A bumper potential is also added that penalizes the formation of interprotomer contacts.

Because each simulated window varies the distance separating the CLC-ec1 protomers, this distance defines the reaction coordinate used when describing the free energy of association. We thus define this separating distance by introducing two sets of atoms from each protomer and computing the geometric center of each set. These centers are shown as G_1 and G_2 in Extended Data Fig. 6a,b, and the specific atoms that make the sets are provided in Supplementary Table 11. Next, a single point is computed for each protomer as the center of points G_1 and G_2. This point defines the center of each protomer and the distance between them is restrained at their initial distance taken when the simulation is started, which, due to the translations described previously, ranges from 3.4 nm to 8.9 nm for the native dimer and 3.8 nm to 9.3 nm for the non-native dimer. The restraints described here consist of harmonic potentials with a force constant of 2,000 kJ mol^{-1} nm^{-2} and are introduced during the simulation using PLUMED[78].

In addition to the separating distance just described, the protein orientation is also maintained by introducing a second set of restraints designed to prevent rotation around the z axis while maintaining fluctuations in the protein tilt angle. Typically, these restraints do not affect the sampling of the internal configurational space. However, they are introduced here to maintain either the native or non-native dimers throughout the simulations. The restraints work by fixing the y-component of the centers G_1 and G_2, that is, these centers are restrained to the XZ plane. An additional center is then computed as the center of the two protomer's geometric centers, that is, this new center defines a point directly between the two subunits and is restrained to a line by holding fixed the x and z components. Both restraints described here are implemented using the upper- and lower-WALLS options available in PLUMED and use a force constant of 2,000 kJ mol^{-1} nm^{-2}.

With the intersubunit distance and the protein orientation fixed, an additional potential, referred to as a bumper potential, is added to our simulations that penalizes the formation of interprotomer contacts. This bumper is needed since we are primarily interested in the membrane's contribution to the association energy. The bumper aids in this task by providing a visual cue in the free energy profile indicating that the subunits are interacting with each other. The bumper is applied using PLUMED and adds a repulsive term based on the minimum distance between the backbone atoms of each protein unit. For our simulations, the CG beads lining the surface of the protein's transmembrane region are selected, resulting in 207 atoms from each protomer. The bumper is then defined using a flat bottom potential of the form:

$$E(\delta_{\min}) = K(\delta_{\min} - \delta_{\text{rep}})^2 \tag{14}$$

where K is the force constant set to 2,000 kJ mol^{-1} nm^{-2}, $\delta_{\min}$ is the minimum distance between the two groups of selected backbone atoms and δ_{rep} is the distance at which the potential activates; this distance is chosen as 1.2 nm, and the protomers are repelled for any minimum distance smaller than this.

Following our umbrella sampling simulation exploring the association of a native dimer in pure POPC, we perform an additional one in a mixture of DLPC and POPC. The initial structure is taken from the last frame of the corresponding simulation in pure POPC, and 30% of the lipids are randomly selected from each leaflet and converted to DLPC. The windows are then simulated for 35 µs, each using the same settings described before. With adequate sampling from each of the three molecular systems, the unbiased potential of mean force is recovered using weighted histogram analysis method[74] (using a publicly available implementation[79]) and the error estimates are computed by splitting the trajectory into five pieces, analyzing each independently, and reporting the s.d. for each data point. When interpreting the potential of mean force, we consider the number of interprotomer contacts formed at each separating distance. This quantity is computed by pooling snapshots from the different windows based on the instantaneous intersubunit distance between subunits. This quantity is normalized by the number of contacts observed in the native dimer (Fig. 6d).

Reporting summary

Further information on research design is available in the Nature Portfolio Reporting Summary linked to this article.

Data availability

The data reported in this study includes total internal reflection fluorescence (TIRF) microscopy images, functional efflux recordings, fluorescence spectra and MD simulation trajectories. Due to file size limitations, raw TIRF images and MD trajectories will be provided after publication upon request to J.L.R. All data will be archived at Washington University. The analyzed source data for the figures in this paper were provided to the journal as Supplementary Information, and a minimal subset of the raw data files, along with FEP parameters and source data files, have been uploaded on the online data repository Zenodo (https://doi.org/10.5281/zenodo.16897514)[80]. Source data are provided with this paper.

Code availability

The code used for analyzing the simulated trajectories described in this study is available online: https://github.com/MOSAICS-NIH/MOSAICS.

References

54. Walden, M. et al. Uncoupling and turnover in a Cl$^-$/H$^+$ exchange transporter. *J. Gen. Physiol.* **129**, 317–329 (2007).
55. Dutzler, R., Campbell, E. B. & MacKinnon, R. Gating the selectivity filter in ClC chloride channels. *Science* **300**, 108–112 (2003).
56. Robertson, J. L., Kolmakova-Partensky, L. & Miller, C. Design, function and structure of a monomeric ClC transporter. *Nature* **468**, 844–847 (2010).
57. Faraldo-Gómez, J. D. & Roux, B. Electrostatics of ion stabilization in a ClC chloride channel homologue from *Escherichia coli*. *J. Mol. Biol.* **339**, 981–1000 (2004).

58. Staritzbichler, R., Anselmi, C., Forrest, L. R. & Faraldo-Gómez, J. D. GRIFFIN: a versatile methodology for optimization of protein–lipid interfaces for membrane protein simulations. *J. Chem. Theory Comput.* **7**, 1167–1176 (2011).
59. Phillips, J. C. et al. Scalable molecular dynamics on CPU and GPU architectures with NAMD. *J. Chem. Phys.* **153**, 044130 (2020).
60. Shaw, D. E. et al. Anton 2: raising the bar for performance and programmability in a special-purpose molecular dynamics supercomputer. In *Proc. International Conference for High Performance Computing, Networking, Storage and Analysis* 41–53 (IEEE, 2014).
61. Best, R. B. et al. Optimization of the additive CHARMM all-atom protein force field targeting improved sampling of the backbone φ, ψ and side-chain χ^1 and χ^2 dihedral angles. *J. Chem. Theory Comput.* **8**, 3257–3273 (2012).
62. Lippert, R. A. et al. Accurate and efficient integration for molecular dynamics simulations at constant temperature and pressure. *J. Chem. Phys.* **139**, 164106 (2013).
63. Jensen, M. Ø. et al. Mechanism of voltage gating in potassium channels. *Science* **336**, 229–233 (2012).
64. Pan, A. C. et al. Atomic-level characterization of protein–protein association. *Proc. Natl Acad. Sci. USA* **116**, 4244–4249 (2019).
65. Bülow, S., von, Bullerjahn, J. T. & Hummer, G. Systematic errors in diffusion coefficients from long-time molecular dynamics simulations at constant pressure. *J. Chem. Phys.* **153**, 021101 (2020).
66. Fukunishi, H., Watanabe, O. & Takada, S. On the Hamiltonian replica exchange method for efficient sampling of biomolecular systems: application to protein structure prediction. *J. Chem. Phys.* **116**, 9058–9067 (2002).
67. Bennett, C. H. Efficient estimation of free energy differences from Monte Carlo data. *J. Comput. Phys.* **22**, 245–268 (1976).
68. Monticelli, L. et al. The MARTINI coarse-grained force field: extension to proteins. *J. Chem. Theory Comput.* **4**, 819–834 (2008).
69. Marrink, S. J., Risselada, H. J., Yefimov, S., Tieleman, D. P. & de Vries, A. H. The MARTINI force field: coarse grained model for biomolecular simulations. *J. Phys. Chem. B* **111**, 7812–7824 (2007).
70. Wassenaar, T. A., Ingólfsson, H. I., Böckmann, R. A., Tieleman, D. P. & Marrink, S. J. Computational lipidomics with insane: a versatile tool for generating custom membranes for molecular simulations. *J. Chem. Theory Comput.* **11**, 2144–2155 (2015).
71. Bekker, H. et al. Gromacs—a parallel computer for molecular-dynamics simulations. In *Proc. 4th International Conference on Computational Physics (PC 92)* (eds DeGroot, R. A. & Nadrchal, J.) 252–256 (World Scientific Publishing, 1993).
72. Berendsen, H. J. C., Postma, J. P. M., Gunsteren, W. F., van, DiNola, A. & Haak, J. R. Molecular dynamics with coupling to an external bath. *J. Chem. Phys.* **81**, 3684–3690 (1984).
73. Bussi, G., Donadio, D. & Parrinello, M. Canonical sampling through velocity rescaling. *J. Chem. Phys.* **126**, 014101 (2007).
74. Kumar, S., Rosenberg, J. M., Bouzida, D., Swendsen, R. H. & Kollman, P. A. THE weighted histogram analysis method for free-energy calculations on biomolecules. I. The method. *J. Comput. Chem.* **13**, 1011–1021 (1992).
75. Ozturk, T. N. et al. Mitigation of membrane morphology defects explain stability and orientational specificity of CLC dimers. Preprint at *bioRxiv* https://doi.org/10.1101/2023.03.16.533024 (2023).
76. Yan, Y., Tao, H., He, J. & Huang, S.-Y. The HDOCK server for integrated protein–protein docking. *Nat. Protoc.* **15**, 1829–1852 (2020).
77. Parrinello, M. & Rahman, A. Polymorphic transitions in single crystals: a new molecular dynamics method. *J. Appl. Phys.* **52**, 7182–7190 (1981).
78. Bonomi, M. et al. PLUMED: a portable plugin for free-energy calculations with molecular dynamics. *Comput. Phys. Commun.* **180**, 1961–1972 (2009).
79. Grossfield, A. WHAM: the weighted histogram analysis method. Version 2.0.10. membrane.urmc.rochester.edu/wordpress/?page_id=126 (2023).
80. Bernhardt, N. et al. Minimal raw dataset and source data files for Bernhardt, et al., NCB, 2025. *Zenodo* https://doi.org/10.5281/zenodo.16897514 (2025).
81. Boerner, T. J., Deems, S., Furlani, T. R., Knuth, S. L. & Towns, J. ACCESS: advancing innovation: NSF's advanced cyberinfrastructure coordination ecosystem: services & support. In *Proc. Practice and Experience in Advanced Research Computing 2023: Computing for the Common Good* 173–176 (ACM, 2023).

Acknowledgements

The Faraldo-Gómez lab was funded by the Division of Intramural Research of the National Heart, Lung, and Blood Institute (NHLBI), National Institutes of Health (NIH). The Robertson lab is supported by the National Institute of General Medical Sciences, NIH (R01GM120260 to J.L.R. and R.C. and R03NS133680 to J.L.R.). This study received funding in whole or in part by the NIH. It is subject to the NIH Public Access Policy. Through acceptance of this federal funding, NIH has been given a right to make this paper publicly available in PubMed Central on the official date of publication. Computing resources were in part provided by the NIH supercomputer Biowulf, Bridges-2 at the Pittsburg Supercomputing Center (PSC) through allocation MCB200217 from the Advanced Cyberinfrastructure Coordination Ecosystem: Services & Support (ACCESS) program[81], which is supported by the U.S. National Science Foundation (grants 2138259, 2138286, 2138307, 2137603 and 2138296). Anton 2 computer time was provided by PSC (through grant R01GM116961) from the NIH through allocation MCB170100P. The Anton 2 machine at PSC was made available by D.E. Shaw Research. We thank F. Marinelli (NHLBI, NIH) for useful discussions on the design of the FEP calculations, as well as K. Struve (University of Iowa) and R. Stix (NHLBI, NIH) for technical help in these studies.

Author contributions

R.C. carried out the experimental studies. The Anton simulation was designed by J.D.F.-G., J.L.R. and A.G.-L., run by A.G.-L. and analyzed by N.B. FEP simulations were designed by J.D.F.-G., N.S. and N.B., and analyzed by N.B. Umbrella sampling simulations were designed by T.N.O., J.D.F.-G., J.L.R. and S.Z., and analyzed by S.Z. Analysis software was designed by N.B. and J.D.F.-G., and coded by N.B. The paper was written by J.L.R., N.B. and J.D.F.-G., and all authors participated in revisions. J.L.R. and J.D.F.-G. conceived of the project, supervised all aspects of the work and obtained funding to support the research.

Competing interests

The authors declare no competing interests.

Additional information

Extended data is available for this paper at https://doi.org/10.1038/s41589-025-02032-w.

Supplementary information The online version contains supplementary material available at https://doi.org/10.1038/s41589-025-02032-w.

Correspondence and requests for materials should be addressed to Janice L. Robertson or José D. Faraldo-Gómez.

Peer review information *Nature Chemical Biology* thanks Robin Corey, Ilya Levental, and Ed Lyman for their contribution to the peer review of this work.

https://doi.org/10.1038/s41589-025-02032-w

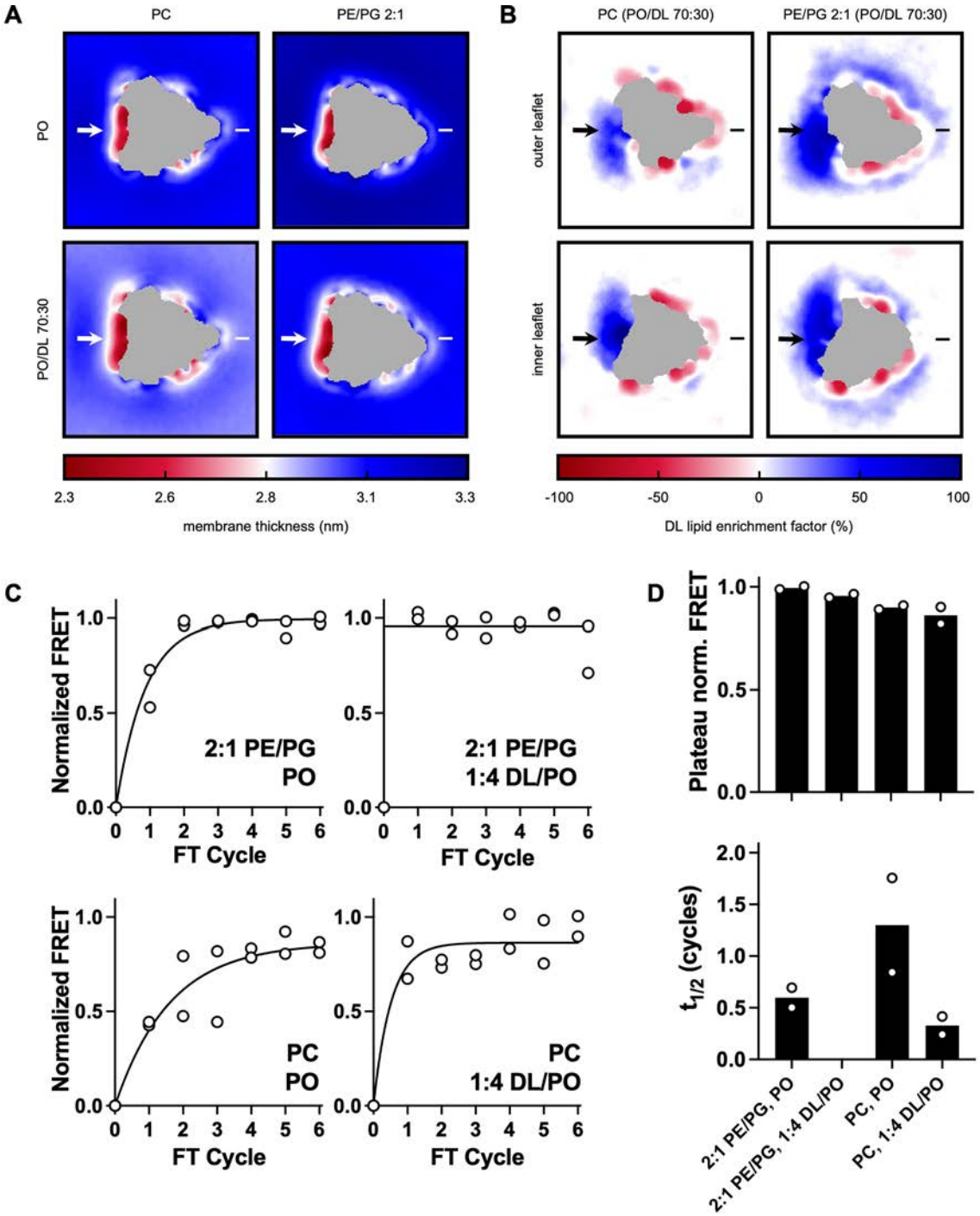

Extended Data Fig. 1 | Comparison of PC and PE/PG membranes. (**a**) Membrane thickness maps from coarse-grained molecular dynamics simulations of the CLC-ec1 monomer in POPC, 70% POPC/30% DLPC, 2:1 POPE/POPG and 70% PO/30% DL in 2:1 PE/PG. PE/PG trajectory data were from ref. 25. (**b**) DL enrichment maps for 70% PO/30% DL simulations in PC vs. 2:1 PE/PG headgroups. Experimental measurements of membrane fusion by ratiometric FRET from 0.02% NBD and 0.1% RhB combined liposomes as a function of freeze/thaw cycle. (**c**) Normalized FRET from liposome samples measured after each freeze/thaw (FT) fusion cycle. The data were normalized between the negative control signal from the combination of NBD and RhB samples prior to fusion (set to 0) and the positive control signal from the NBD/RhB co-labeled liposomes (set to 1). Data is represented explicitly for n = 2 biological replicates. Data were fit to a single exponential association function to estimate the (**d**) plateau FRET and half-time ($t_{1/2}$) for maximal fusion as a function of freeze/thaw cycles. Data represented as the mean over n = 2 biological replicates, with explicit data points overlaid as scatter points.

https://doi.org/10.1038/s41589-025-02032-w

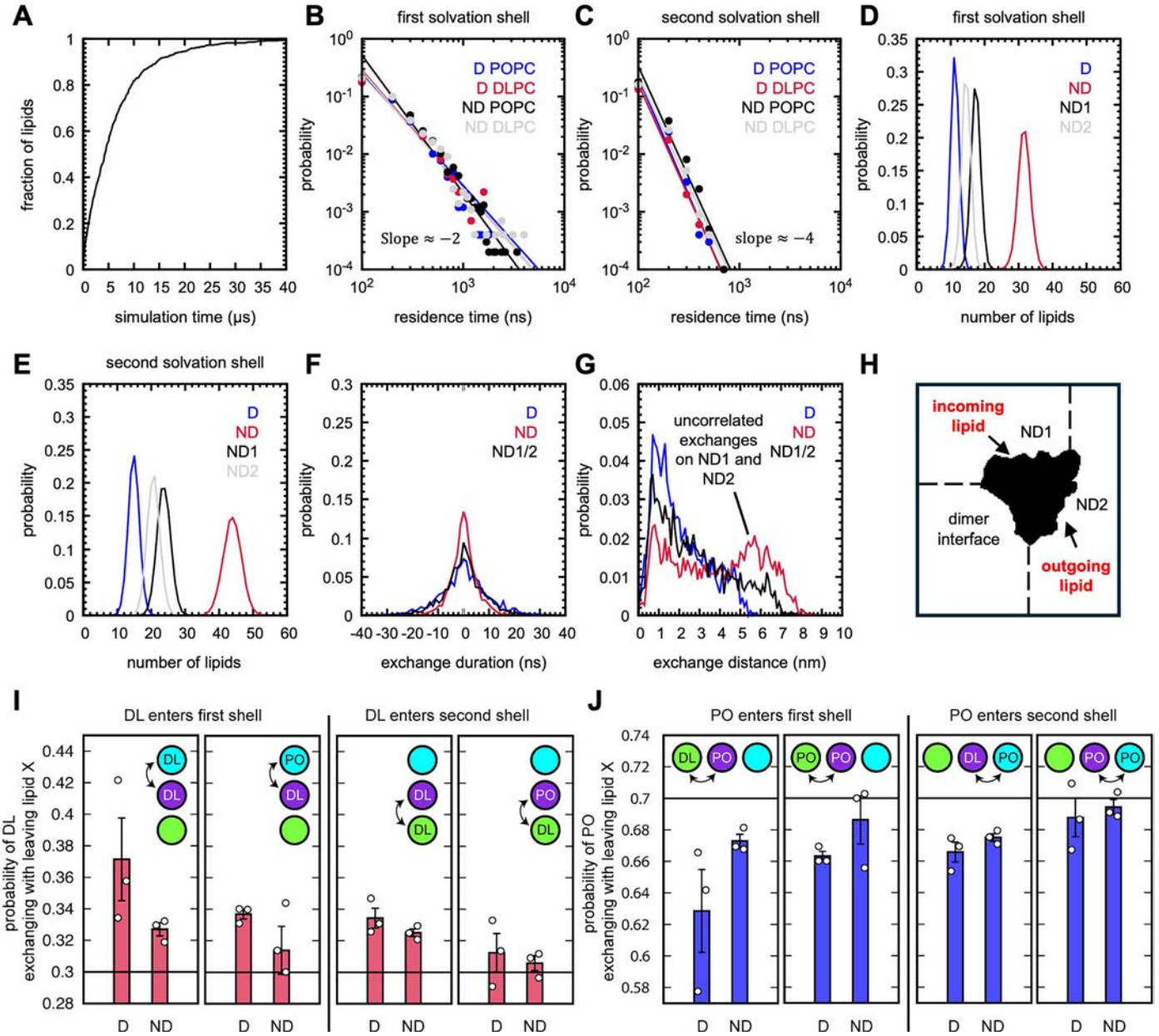

Extended Data Fig. 2 | Characterization of lipid dynamics in the 1st and 2nd solvation shells of a CLC-ec1 monomer from all-atom molecular dynamics simulations. (**a**) Fraction of lipids to visit the inner solvation shell of the protein for at least 100 ns computed as a function of simulation time. Data averaged over the inner and outer leaflets. (**b**) Distribution of dwell times for lipids located in CLC's 1st or (**c**) 2nd solvation shells, at dimerization (D) and non-dimerization (ND) interfaces. Dwell times decay according to a power law with indicated exponent. Probability that the protein's first (**d**) or second solvation shell (**e**), or a segment of these shells lying adjacent to the dimerization or non-dimerization interface, contains a varying number of lipids. The non-dimerization interface is subdivided into two segments, ND1 and ND2, when analyzing lipid exchanges (Fig. 1a) and the number of lipids occupying these segments is also provided. The number of lipids shown is for a single leaflet, averaged over the inner and outer leaflets. (**f**) The time taken for lipid exchanges as measured by subtracting when a lipid leaves the solvation shell from the time at which the incoming lipid arrives. (**g**) The distance between exchange partners. The peak corresponding to uncorrelated events is indicated. (**h**) Due to the size and shape of the non-dimerization interface, we split it into 2 equally sized sections as indicated with the dashed lines and labels ND1 and ND2. By performing the lipid exchange analysis on ND1 and ND2 separately, uncorrelated events, like the example shown here with arrows, are removed. This is seen by a reduction in the peak centered at 6 nm in panel **g**. (**i**) Probability of DL exchanging with a leaving lipid (X = DL or PO) for the first (cyan) and second (purple) solvation shells like shown in Fig. 4i. Data represent mean ± SEM for n = 3 technical replicates, obtained by splitting the full trajectory into 3×13.3 μs non-overlapping segments and calculating the mean residence time from each individual segment (overlaid scatter points). For comparison (**j**), the probability is shown when PO exchanges with a leaving lipid (mean ± SEM for n = 3 technical replicates).

https://doi.org/10.1038/s41589-025-02032-w

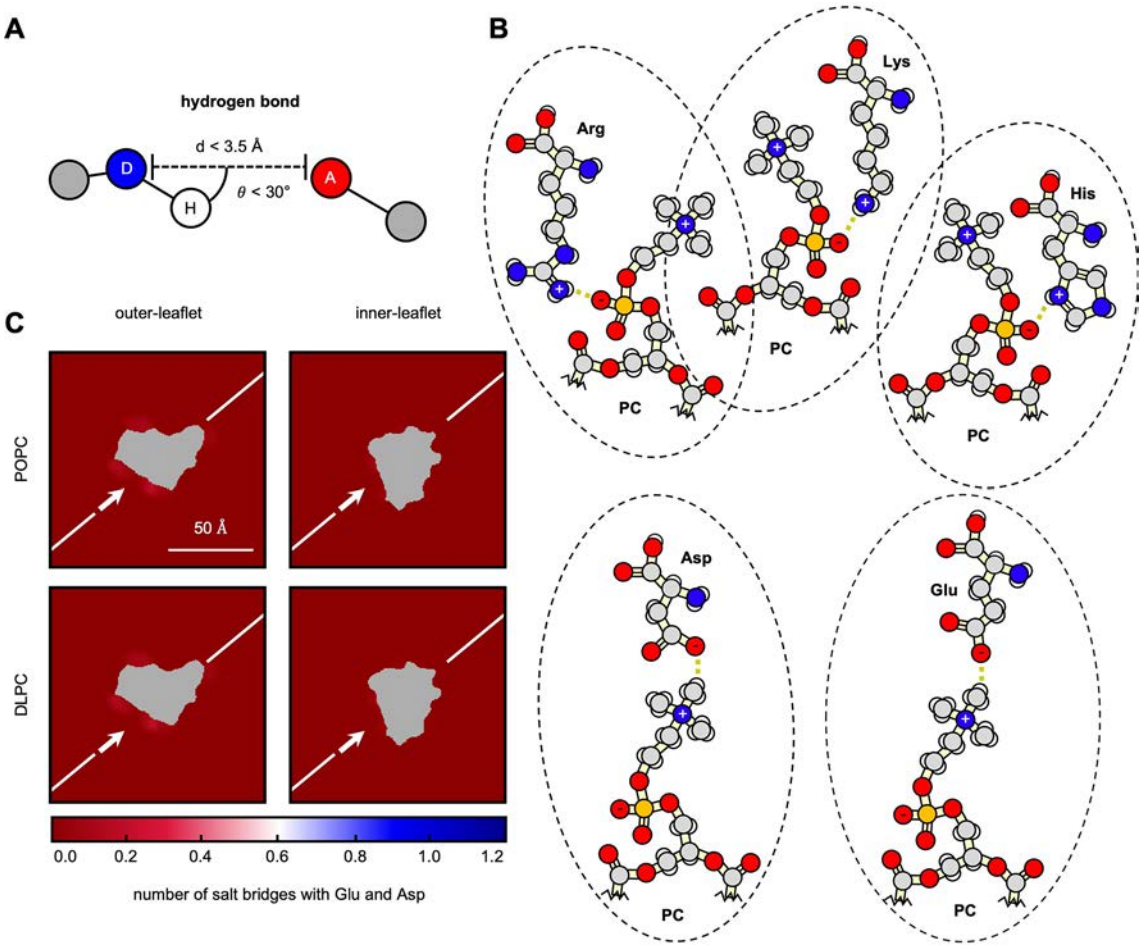

Extended Data Fig. 3 | Counting salt bridges between lipids and the CLC-ec1 subunit. (**a**) The angle between donor, acceptor, and hydrogen atoms used when counting hydrogen bonds. The cutoff angle and distance are 30° and 3.5 Å, respectively. (**b**) Salt bridges are counted as select hydrogen bonds between POPC/DLPC molecules and charged amino acids Arginine (Arg), Lysine (Lys), Histidine (His), Glutamate (Glu), and Aspartic acid (Asp). (**c**) The number of salt bridges formed between the choline group and negatively charged residues Glu and Asp. These interactions are weak due to the many electron-donating methyl groups found on choline and are thus excluded in our main analysis of salt bridges (Fig. 4f).

https://doi.org/10.1038/s41589-025-02032-w

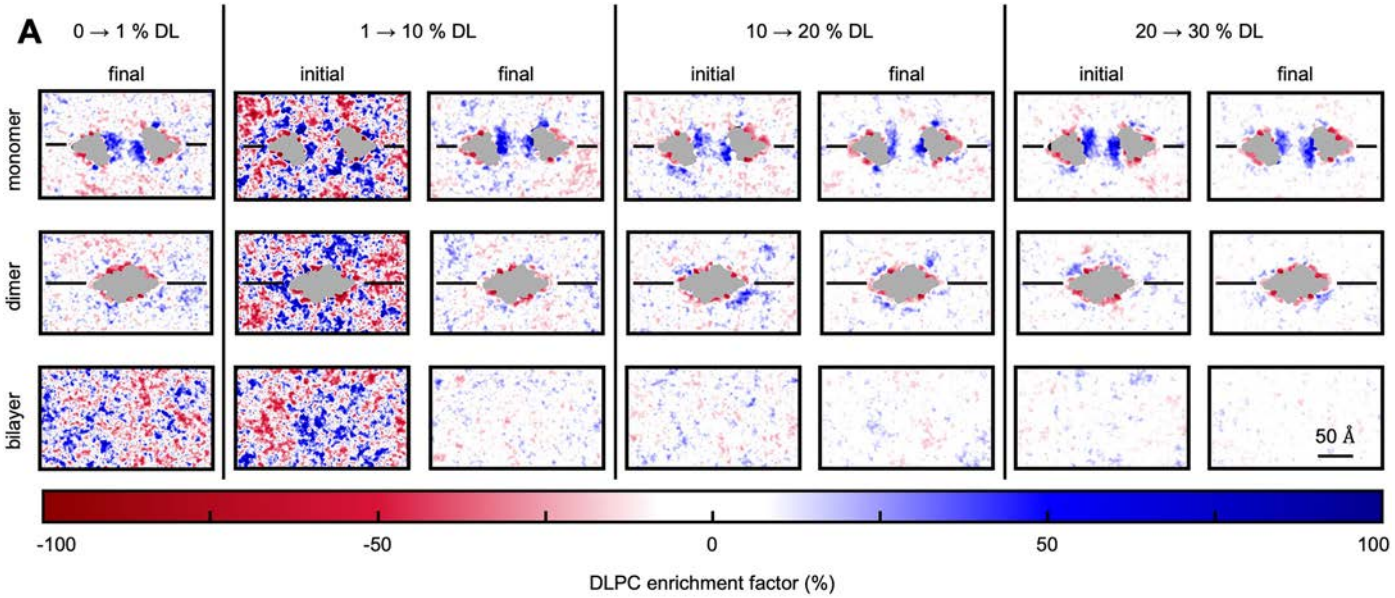

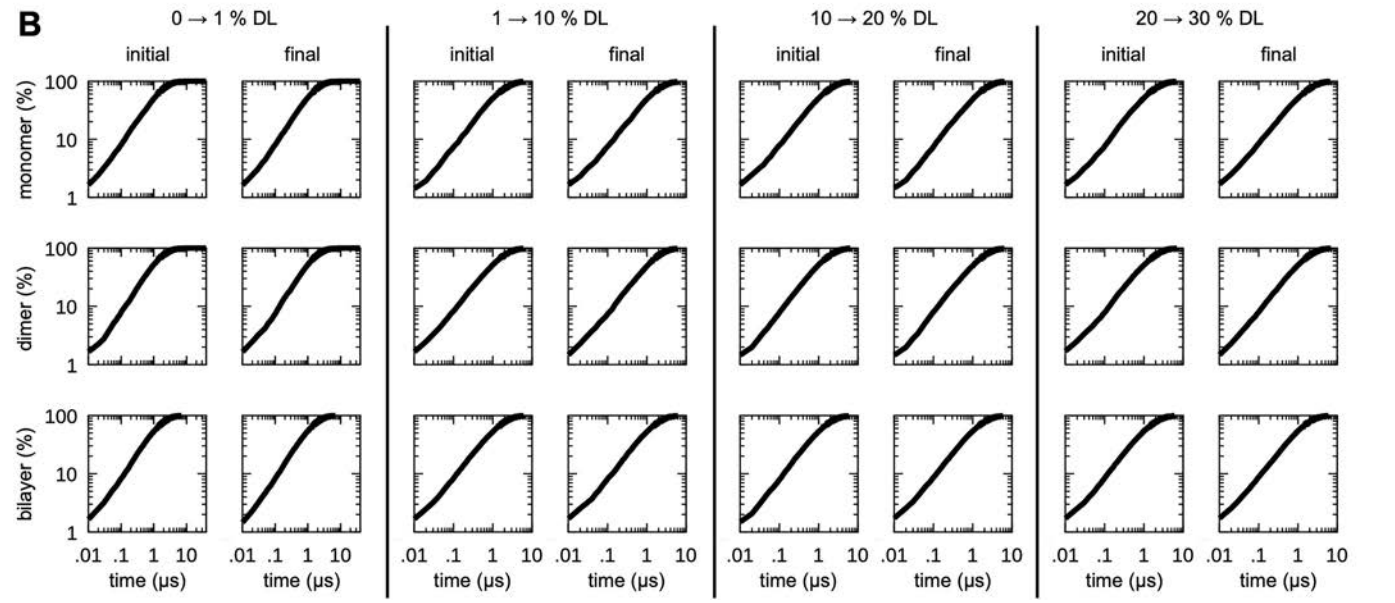

Extended Data Fig. 4 | Evaluation of lipid mixing in free energy perturbation simulations. (**a**) Two-dimensional projection of the enrichment factor shown for the outer leaflet only and for the initial and final states of each transformation, where the initial state corresponds to lambda 0 and the final state lambda 1. For convenience, data is shown for the forward path only. Gray regions represent low lipid density that roughly corresponds to the protein's location. No data is shown for the initial state of the first transformation since no DLPC lipids are present and thus the enrichment factor is undefined. (**b**) The fraction of lipids in the molecular system to visit the inner solvation shell of each lipid as the simulation progresses. A cutoff distance of 1.1 nm is used for identifying first shell lipids. Data is averaged over all lipids in the molecular system at each timepoint.

https://doi.org/10.1038/s41589-025-02032-w

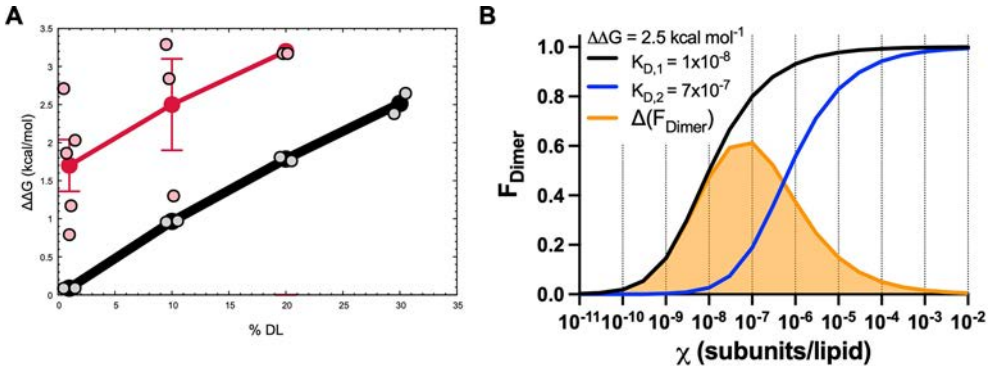

Extended Data Fig. 5 | Free energy changes associated with CLC-ec1 dimerization as a function of PO/DL lipid mixtures. (**a**) $\Delta\Delta G$ determined from free energy perturbation calculations (black) is compared to free energy changes measured from single-molecule photobleaching experiments of CLC-ec1 dimerization stability in 2:1 PE/PG lipid bilayers as a function of % DL vs. PO (red, experimental data from ref. 25). It is noted that the molecular systems simulated here contain a lipid-to-protein ratio that is ≈1,000 times smaller than the experimental system. The implication is that the number of DL lipids available to solvate each protein molecule is much greater under experimental conditions, and the inhibitory effect of DL is necessarily more pronounced in experiment. To compare with simulation, we factor out this size effect by comparing the calculated and experimental free-energy changes in reference to the largest DL molar fraction studied, that is, the condition in which the DL enrichment is not limited by the number of DL lipids available, in either protein state. Thus, comparing changes relative to the 20% DL condition (Fig. 5e) shows the agreement between calculated and measured shifts in the dimerization free-energies. For the experimental results, data represents mean ± SEM (red) for 1% and 10% DL, with n = 5 and n = 3 biological replicates, respectively. For 20% DL, n = 2, and so the data is shown as the average and individual scatter points (pink). For the FEP calculations, the values obtained from simulating the forward and backward paths represent n = 2 technical replicates and are shown as gray dots. The black trace follows the average of the two paths. (**b**) Example dimerization isotherms corresponding to CLC-ec1 association in PO membranes (for example, $K_{D,1} = 1 \times 10^{-8}$ subunits/lipid) and DL/PO membranes (for example, $K_{D,2} = 7 \times 10^{-7}$ subunits/lipid), reflecting a $\Delta\Delta G = 2.5$ kcal mol^{-1} change in association stability. The difference in dimerization between these two curves as a function of mole fraction (χ subunits/lipid), showing how the protein population is expected to change between dimers and monomers because of the change in lipid composition, and as a function of expression density.

https://doi.org/10.1038/s41589-025-02032-w

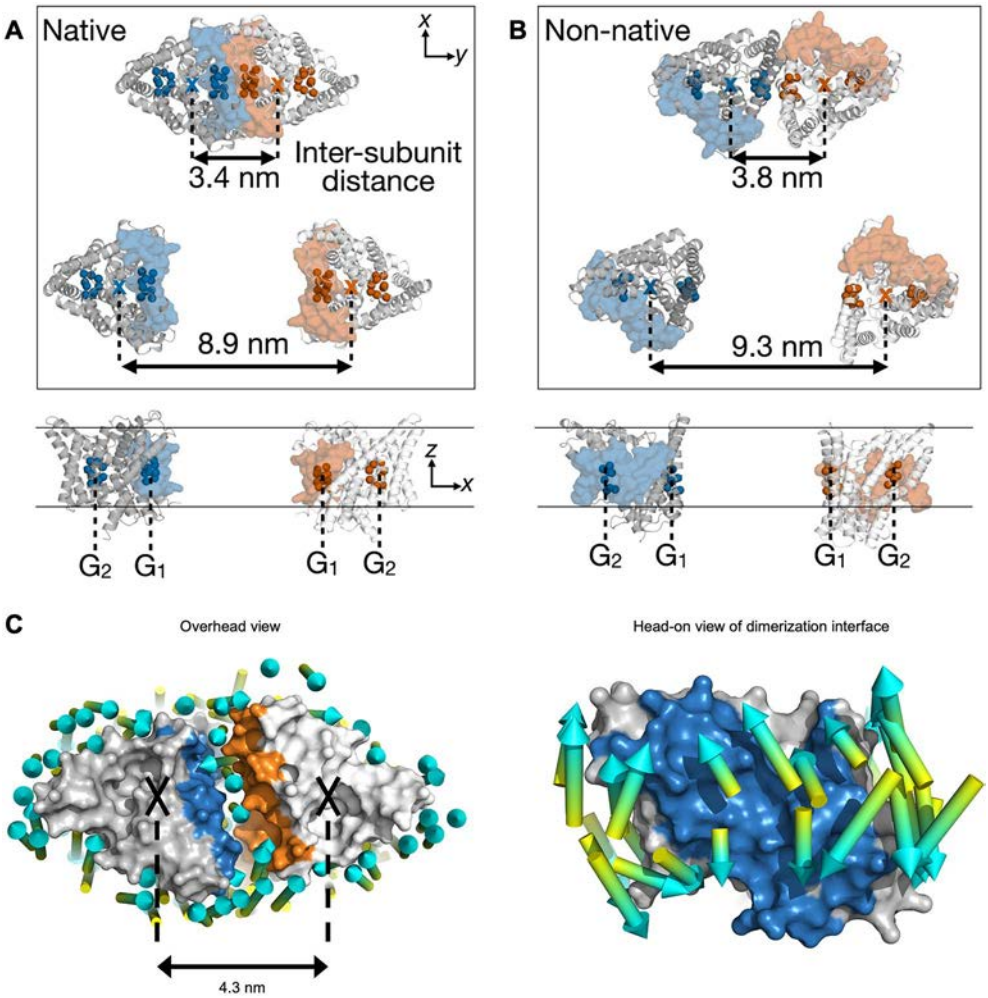

Extended Data Fig. 6 | Reaction coordinate used to restrain intersubunit distance in umbrella sampling simulations and an example taken from the trajectory. (**a**) Native and (**b**) non-native dimer models shown from the extracellular side of the membrane (top) and within the membrane core (bottom). CLC-ec1 protomers are displayed in cartoon representation, colored white and gray. Four transmembrane helices forming the native dimerization interface are overlaid as a transparent surface in orange and blue. In each protomer, alpha carbons of residues used in the inter-subunit distance calculation are shown, represented as orange or blue spheres. Backbone beads of residues were grouped into four centers (G1 and G2 per promoter) and used for defining the restraints that kept the inter-subunit distance at a fixed value while ensuring that dimerization interfaces of two subunits always face each other. Lists of these residues for the native and non-native dimer models are presented in Supplementary Table 11. (**c**) Snapshot taken from the umbrella sampling simulations of the native dimer in POPC where the distance separating the protein centers is consistent with the free energy minimum, that is a distance of 4.3 nm. This snapshot shows a single layer of lipids with reduced packing density remains between the protomers and is consistent with other states of the same separating distance. The lipid vectors are plotted to depict actual lipid densities around the protein.

https://doi.org/10.1038/s41589-025-02032-w

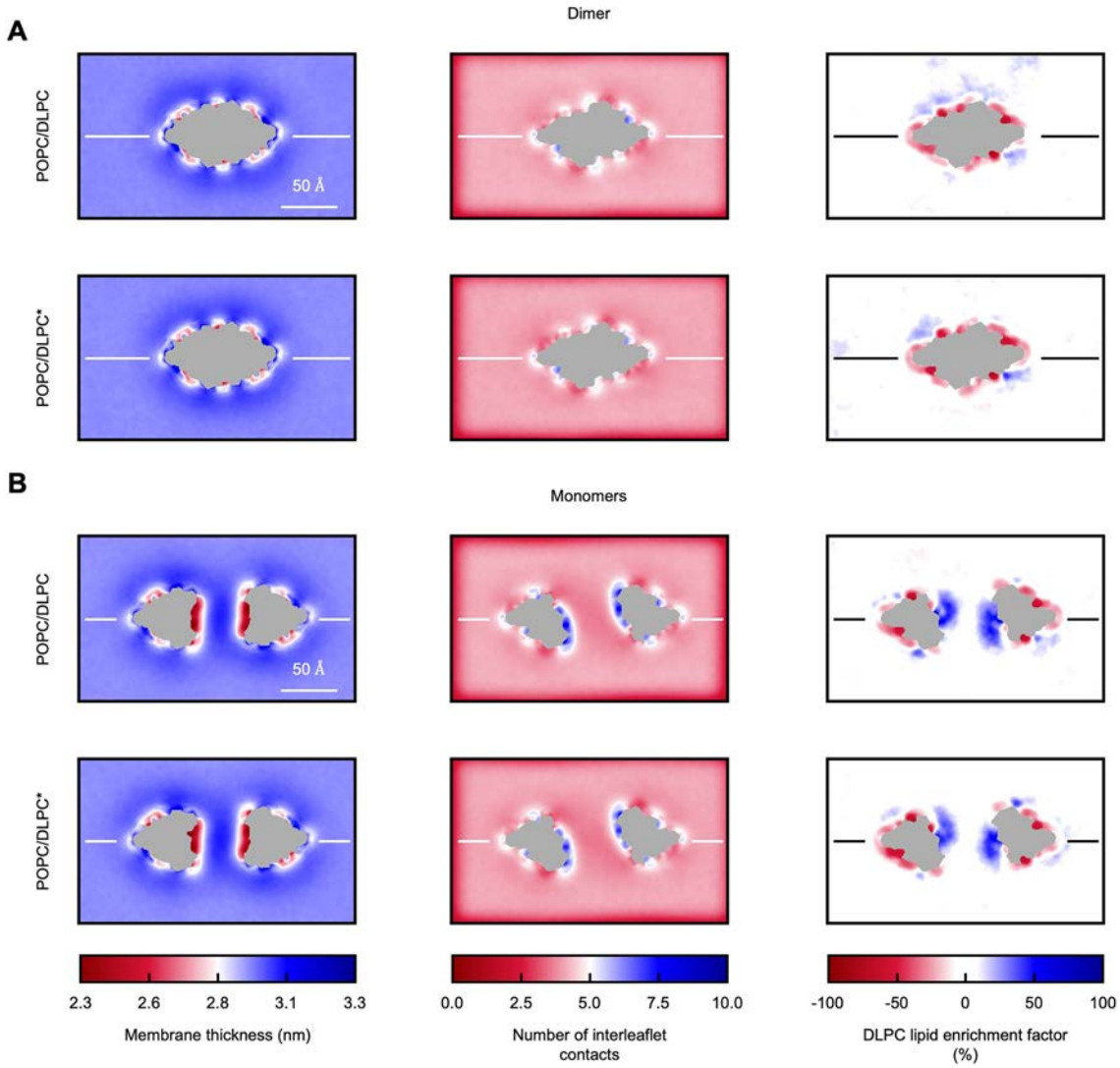

Extended Data Fig. 7 | Properties of dummy DLPC* molecules used in FEP simulations compared to native DLPC. FEP methodology is built on the assumption that the phase space dimensions are unaffected by a given transformation, that is, the number of atoms does not change. In cases where one or more atoms are deleted, this limitation is circumvented by introducing dummy atoms, whose through space interactions are muted (that is, set to zero). For our simulations, we create a modified DLPC molecule, referred to as DLPC*, that is identical to the original DLPC but with a dummy atom attached to the end of each alkyl chain. These added beads are given standard bonding and angle bending parameters and Lennard-Jones terms are set to nil. (**a**) Three metrics are compared for the associated CLC-ec1 dimer systems containing a mixture of POPC and native DLPC molecules and systems containing POPC and DLPC*: (left) membrane thickness, (middle) number of interleaflet contacts (outer leaflet only), and (right) DLPC enrichment factor (outer leaflet only). (**b**) Same analysis as in (**a**) but for the dissociated monomers.

https://doi.org/10.1038/s41589-025-02032-w

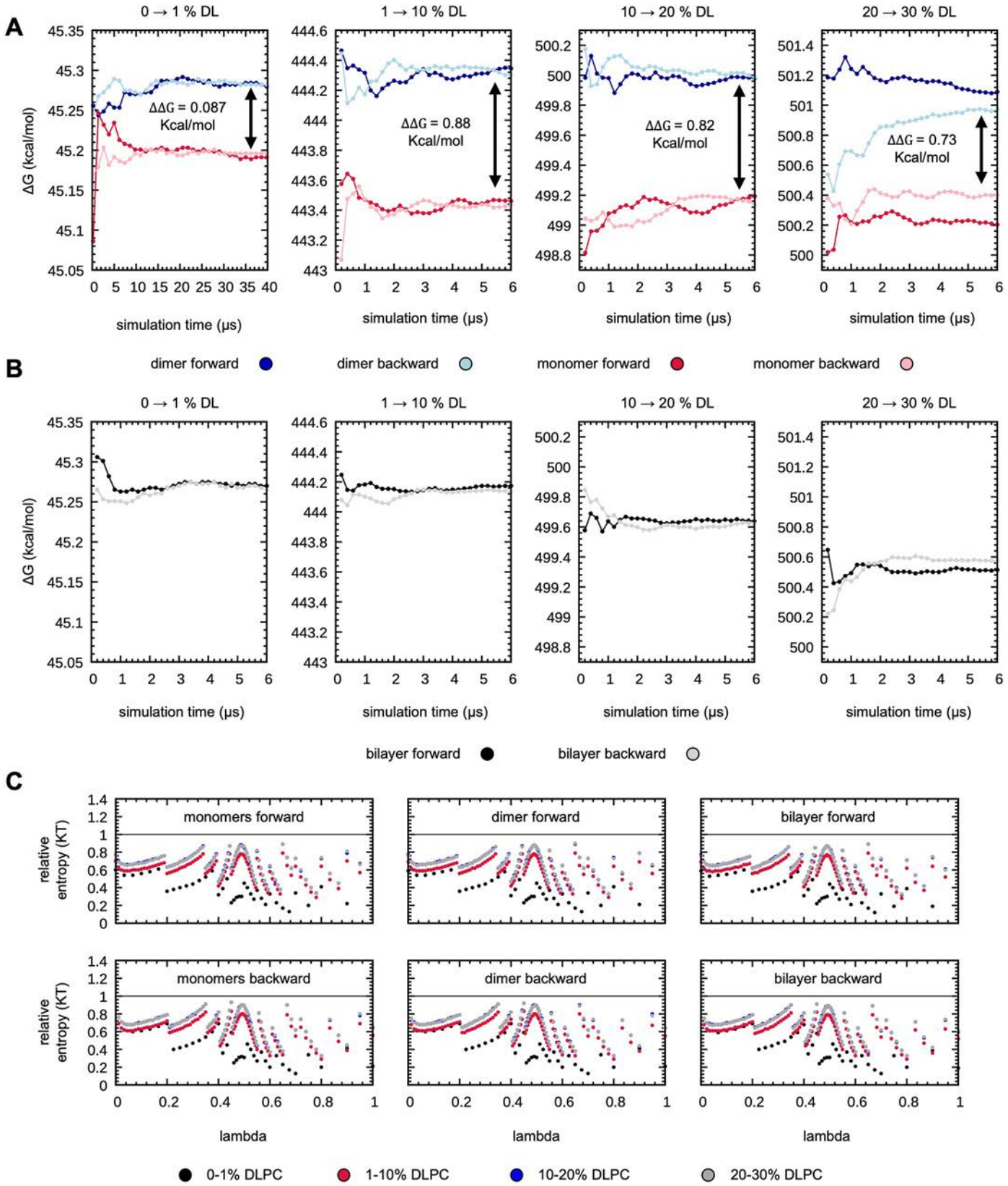

Extended Data Fig. 8 | Convergence of free energy perturbation simulations. (**a**) Estimated free energy cost to transform POPC molecules into DLPC monitored over the course of the free energy perturbation simulations. The transformations were performed for a molecular system containing a lipid bilayer with an embedded CLC dimer in the associated or dissociated states. Data is shown for the forward and backward paths, which tend toward a common value when sufficient sampling is obtained. The free energy difference between transformations carried out in the associated and dissociated states is indicated by vertical arrows. (**b**) Same as (**a**) but for a protein-free lipid bilayer. (**c**) Lambda values are selected to ensure overlap between the probability distributions of neighboring replicas, where overlap is considered sufficient when the pair's relative entropy is less than 1 k_BT. Entropy values are shown for replicas, whose lambda value is given on the x-axis, and the neighbor to the right for the forward path or left for the backward path.

nature portfolio

Corresponding author(s): Janice L. Robertson
Jose D. Faraldo-Gomez

Last updated by author(s): Aug 20, 2025

Reporting Summary

Nature Portfolio wishes to improve the reproducibility of the work that we publish. This form provides structure for consistency and transparency in reporting. For further information on Nature Portfolio policies, see our Editorial Policies and the Editorial Policy Checklist.

Statistics

For all statistical analyses, confirm that the following items are present in the figure legend, table legend, main text, or Methods section.

n/a	Confirmed
☐	☒ The exact sample size (*n*) for each experimental group/condition, given as a discrete number and unit of measurement
☐	☒ A statement on whether measurements were taken from distinct samples or whether the same sample was measured repeatedly
☐	☒ The statistical test(s) used AND whether they are one- or two-sided *Only common tests should be described solely by name; describe more complex techniques in the Methods section.*
☒	☐ A description of all covariates tested
☒	☐ A description of any assumptions or corrections, such as tests of normality and adjustment for multiple comparisons
☐	☒ A full description of the statistical parameters including central tendency (e.g. means) or other basic estimates (e.g. regression coefficient) AND variation (e.g. standard deviation) or associated estimates of uncertainty (e.g. confidence intervals)
☐	☒ For null hypothesis testing, the test statistic (e.g. *F*, *t*, *r*) with confidence intervals, effect sizes, degrees of freedom and *P* value noted *Give P values as exact values whenever suitable.*
☒	☐ For Bayesian analysis, information on the choice of priors and Markov chain Monte Carlo settings
☒	☐ For hierarchical and complex designs, identification of the appropriate level for tests and full reporting of outcomes
☒	☐ Estimates of effect sizes (e.g. Cohen's *d*, Pearson's *r*), indicating how they were calculated

Our web collection on statistics for biologists contains articles on many of the points above.

Software and code

Policy information about availability of computer code

Data collection	Gromacs 2018.8, NAMD 2.12
Data analysis	MOSAICS v1.1.0 (https://github.com/MOSAICS-NIH/MOSAICS), WHAM

For manuscripts utilizing custom algorithms or software that are central to the research but not yet described in published literature, software must be made available to editors and reviewers. We strongly encourage code deposition in a community repository (e.g. GitHub). See the Nature Portfolio guidelines for submitting code & software for further information.

Data

Policy information about availability of data

All manuscripts must include a data availability statement. This statement should provide the following information, where applicable:

- Accession codes, unique identifiers, or web links for publicly available datasets
- A description of any restrictions on data availability
- For clinical datasets or third party data, please ensure that the statement adheres to our policy

The data reported in this study includes total internal reflection fluorescence (TIRF) microscopy images, functional efflux recordings, fluorescence spectra and molecular dynamics (MD) simulation trajectories. Due to file size limitations, raw TIRF images and MD trajectories will be provided after publication upon request to Janice L. Robertson (janice.robertson@wustl.edu). All data will be archived at Washington University. The analyzed source data for the figures in this paper were

provided to the journal as Supplementary Information, and a minimal subset of the raw data files, along with FEP parameters and source data files have been uploaded on the online data repository Zenodo (https://doi.org/10.5281/zenodo.16897514)34 .

Research involving human participants, their data, or biological material

Policy information about studies with human participants or human data. See also policy information about sex, gender (identity/presentation), and sexual orientation and race, ethnicity and racism.

Reporting on sex and gender	Not applicable.
Reporting on race, ethnicity, or other socially relevant groupings	Not applicable.
Population characteristics	Not applicable.
Recruitment	Not applicable.
Ethics oversight	Not applicable.

Note that full information on the approval of the study protocol must also be provided in the manuscript.

Field-specific reporting

Please select the one below that is the best fit for your research. If you are not sure, read the appropriate sections before making your selection.

☒ Life sciences ☐ Behavioural & social sciences ☐ Ecological, evolutionary & environmental sciences

For a reference copy of the document with all sections, see nature.com/documents/nr-reporting-summary-flat.pdf

Life sciences study design

All studies must disclose on these points even when the disclosure is negative.

Sample size	Biological replicate sample sizes were selected based on error analysis from previous studies, which have shown than n => 3 allows for the measurement of significant differences in photobleaching probability distributions and oligomeric populations between different proteoliposome conditions (see Chadda et al., eLife 2016, Chadda, Bernhardt et al., eLife 2021 and Chadda, Lee et al., PNAS 2023).
Data exclusions	No data were excluded.
Replication	For experimental studies, the measurements were repeated with independently purified, labeled and reconstituted protein constituting distinct biological replicates. For all of the photobleaching studies and functional measurements n >= 3. For the computational calculations, we examined the convergence and sampling variability by splitting trajectories into 3 separate segments, calculating the analyzed metric from each segment and reporting the mean +/- standard error on the mean as a measure of reproducibility.
Randomization	Not applicable.
Blinding	The experimental studies were not blinded as a single scientist carried out these measurements.

Reporting for specific materials, systems and methods

We require information from authors about some types of materials, experimental systems and methods used in many studies. Here, indicate whether each material, system or method listed is relevant to your study. If you are not sure if a list item applies to your research, read the appropriate section before selecting a response.

Materials & experimental systems

n/a	Involved in the study
☒	☐ Antibodies
☒	☐ Eukaryotic cell lines
☒	☐ Palaeontology and archaeology
☒	☐ Animals and other organisms
☒	☐ Clinical data
☒	☐ Dual use research of concern
☒	☐ Plants

Methods

n/a	Involved in the study
☒	☐ ChIP-seq
☒	☐ Flow cytometry
☒	☐ MRI-based neuroimaging

Plants

Seed stocks	Not applicable.
Novel plant genotypes	Not applicable.
Authentication	Not applicable.